

1 **Assessing the plausibility of direct constraints on ancient atmospheric pCO₂ from fluid**
2 **inclusions in halite: A theoretical and experimental approach**

3 Michael Naylor Hudgins^{1,2}, Justin G. Park^{1,2}, Alex M. Ryan^{1,2,3}, Jessika A. Rogers^{4,5}, and
4 Morgan F. Schaller^{1,2*}

5 ¹Department of Earth and Environmental Sciences, Rensselaer Polytechnic Institute, Troy,
6 NY, USA.

7 ²Center for Environmental and Stable Isotope Analysis, Rensselaer Polytechnic Institute,
8 Troy, NY, USA.

9 ³Department of Mechanical, Aerospace, and Nuclear Engineering, Rensselaer Polytechnic
10 Institute, Troy, NY, USA.

11 ⁴The Howard P. Isermann Department of Chemical and Biological Engineering, Rensselaer
12 Polytechnic Institute, Troy, NY, USA.

13 ⁵Department of Physics, Applied Physics, and Astronomy, Rensselaer Polytechnic Institute,
14 Troy, NY, USA.

15 This manuscript is a preprint and will be submitted for publication in *Geochimica et*
16 *Cosmochimica Acta*. Take into consideration that the manuscript has yet to be formally accepted
17 for publication and may have slightly different content between the preprint and accepted
18 version. The final version of this manuscript will be available via the publication DOI link.
19 Please feel free to contact any of the authors.

20 **Abstract**

21 Fluid inclusions in halite formed in surficial environments have recently gained attention for
22 their ability to capture and preserve samples of ancient air, and by mechanical decrepitation,
23 these inclusion gases can be quantified via mass spectrometry. However, it has yet to be
24 demonstrated that the CO₂ content measured on halite accurately represents the overlying air at
25 various CO₂ concentrations and not the exsolution of some or all of the dissolved inorganic
26 carbon. Based on the kinetics of the carbonate system equilibrium and aqueous solubility of CO₂,
27 we hypothesize that the CO₂ measured by bulk analysis of fluid inclusion gas is derived solely
28 from a mixture between CO_{2(g)} and [CO₂]_{aq} (CO₂ from air and air-saturated brine). To address
29 this, we first conducted depressurization experiments on atmospherically equilibrated carbonate
30 solutions, and by mass balance we show that only CO_{2(aq)} degasses during solution
31 depressurization, while the remaining HCO₃⁻ and CO₃²⁻ combine with Na⁺ cations to precipitate
32 NaHCO₃ salt. In addition, we performed mechanical decrepitation experiments on lab-grown
33 halite (LGH) that was precipitated in a sealed pressure vessel under various pCO₂ conditions
34 (450 ppm, 3000 ppm, and 5000 ppm). Volatile contents of the carbonate solutions and the LGH
35 were analyzed with a quadrupole mass spectrometer. Measured CO₂ content falls between the
36 expected values of air and air-saturated brine for the different pCO₂ conditions, and by
37 partitioning the gas contributions from each phase, we observe atmospheric pCO₂ that closely
38 matches the starting conditions. Our findings demonstrate that inclusions in halite faithfully
39 entrap and preserve CO₂ from the overlying atmosphere and that the exsolution of DIC does not
40 meaningfully contribute to the measured CO₂, giving confidence in applying our methods to new
41 and existing analyses of both modern and ancient natural halite. Bulk gas analysis of fluid
42 inclusions is one of the only methods to directly constrain ancient atmospheric composition
43 through deep time and extend the record of atmospheric pCO₂ well beyond the ice cores.

Keywords: Fluid Inclusions, Earth's Ancient Atmosphere, CO₂, Halite

*Corresponding author at: Department of Earth and Environmental Sciences, Rensselaer Polytechnic Institute, Troy, NY, USA. *Email address:* judgim@rpi.edu and schall@rpi.edu

1. Introduction

Understanding Earth's climate history depends on reconstructing past atmospheric CO₂ concentrations, which relies on indirect geochemical proxies for time periods prior to the ice core record. (Petit et al., 1999; Schaller et al., 2015; CenCO2PIP, 2023). In ancient systems, proxy methods used to estimate pCO₂ (e.g., the $\delta^{13}\text{C}$ of pedogenic carbonates and leaf stomatal indices) often show similar trends over the same time interval, but disagree in absolute value (c.f. McElwain et al., 1999; Schaller et al., 2011). Despite these and similar inconsistencies, many of the proxy methods show the expected coherent relationship between relative pCO₂ and temperature on geological timescales, indicating that they are precise but ultimately inaccurate (Knobbe and Schaller, 2018; Tierney et al., 2020; Judd et al., 2024). Addressing this inaccuracy requires a more direct measurement of ancient atmospheric CO₂, such as analyses of fluid inclusions hosted in halite that contains actual samples of ancient air. Halite forms in both modern and ancient surficial environments and recent measurements have demonstrated that gases contained within the fluid inclusions in these samples are a direct and high-fidelity archive of Earth's atmospheric composition that may be extended to time periods prior to the ice core record (Pettitt et al., 2020; Park and Schaller, 2025; Park et al., In Review). In addition, isotopic analyses of inclusion gases provide direct constraints on Earth's atmospheric evolution and large scale planetary processes (Sano and Pillinger, 1990; Marty et al., 2013; Avicé et al., 2018). Inclusion analysis of halite can be used to validate and refine existing CO₂ proxy records, however, accurate interpretations of inclusion gases require consideration of phase chemistry (Park and Schaller, 2025).

Major atmospheric gases contained within fluid inclusions (e.g., N₂, O₂, Ar, and CO₂) are quantified via mass spectrometry through mechanical decrepitation under high-vacuum (Graney and Kesler, 1995; Williams, 1996; Norman and Blamey 2001; Pettitt and Schaller, 2020). Within the past decade, the gas compositions from Proterozoic and Phanerozoic halite have provided direct constraints on ancient atmospheric composition (Blamey et al., 2016; Steadman et al., 2020; Brand et al., 2021). However, these studies have garnered criticism for interpreting raw results (Yeung, 2017; Mills et al., 2023), and in particular not partitioning the gaseous from the aqueous phases of their analysis (Park and Schaller, 2025). For example, based on analyses of halite from the 815 Ma Browne Formation, Blamey et al. (2016) report that the oxygen content of the Neoproterozoic atmosphere averaged 10.9% (assuming 1 bar total pressure), which implies that substantial atmospheric oxygenation had occurred ~200 Ma before what is indicated by model predictions and paleo proxies (Lyons et al., 2014; Catling and Zahnle, 2020). In a re-analysis of these data, Yeung (2017) argued that the original measured volatiles are a combination of ancient atmosphere, air-saturated brine, and contamination from the modern atmosphere, concluding that the data is more consistent with an atmosphere of 1.3% O₂. Most importantly, Blamey et al. (2016) explicitly assume that the volatiles released in their original analysis are entirely from air bubbles within the inclusions, and that the aqueous phase is negligible. However, ignoring the aqueous phase of fluid inclusions leads to an erroneous interpretation of the overlying atmospheric composition because the ratios of the individual gaseous components of the atmosphere are notably different from their aqueous counterparts at equilibrium, due to the different solubility of each gas (Yeung, 2017; Pettitt et al., 2020). Park

and Schaller (2025) resolved this problem by developing a gas-aqueous partitioning method for fluid inclusion data to apportion the atmospheric volatiles between the gaseous and aqueous phases and determine the equilibrium atmosphere under which the sample had formed. Park and Schaller's (2025) partitioning method was validated using modern halite samples and was applied to Blamey et al.'s (2016) data, resulting in an average O₂ composition of 6.62%. Gas-aqueous phase partitioning is an essential step in interpreting inclusion gas analyses.

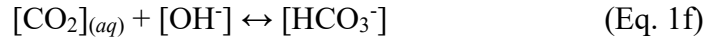
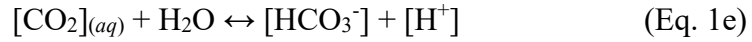
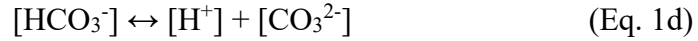
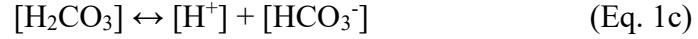
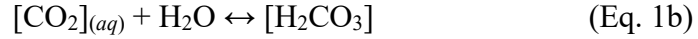
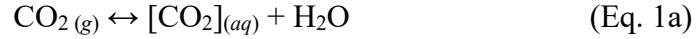
The bulk volatile analysis of fluid inclusion gas has changed our understanding of the biogeochemical cycling of atmospheric volatiles. However, results generated by this new technique have raised many theoretical and fundamental geochemical questions that, to our surprise, have not been addressed in the literature to date. The current study was inspired by a discussion between the authors and a colleague at the 2023 AGU Annual Meeting on whether the measured CO₂ from bulk gas analysis of inclusions represents [CO₂]_{aq} (as we assumed), or some or all of the Total Dissolved Inorganic Carbon (TDIC) in solution (Hudgins et al., 2023). Delving further into this topic, we found that even basic questions like "what happens to CO_{2(aq)} and HCO₃⁻ when a solution is rapidly exposed to high vacuum?" have not been addressed. Answering this question is critical for determining whether CO₂ content measured on fluid inclusions truly represents the equilibrium between a brine and the overlying air during mineral formation. Other studies have recognized this problem (Hudgins et al., 2024; Park and Schaller, 2025), and Pettitt et al. (2020) assumed that the measured CO₂ from palustrine cherts from the Petrified Forest National Park (215 Ma) represents TDIC and not a mix between CO_{2(g)} and [CO₂]_{aq} (air and air-saturated brine CO₂). During analysis, inclusions hosted in minerals are mechanically decrepitated to release trapped volatiles into a high vacuum environment (10⁻⁷ to 10⁻⁸ mbar). Rapid exposure to pressures far below the vapor pressure of the liquid leads to fluid vaporization on millisecond timescales. Pettitt et al. (2020) assumed that the dissolved carbonate species (HCO₃⁻ and CO₃²⁻) underwent protonation and dehydration reactions before exsolving into CO₂ gas during fluid vaporization. However, this assumption is unverified, and other studies hint that the majority of the HCO₃⁻ and CO₃²⁻ precipitate as a carbonate salt during rapid depressurization by combining with dissolved metal cations (Cui et al., 2001; McSween et al. 2003).

In this study, we test whether the CO₂ content measured from bulk gas analysis in fluid inclusions accurately represents the overlying air at various pCO₂ levels during mineral formation, rather than the exsolution of some or all the TDIC. We hypothesize that the fluid inclusions in halite faithfully record the atmospheric conditions under which the mineral precipitated, and that the measured CO₂ content is derived solely from a mixture of CO₂ in air and [CO₂]_{aq} from air-saturated brine. We predict that an insignificant amount of HCO₃⁻ and CO₃²⁻ will exsolve into CO₂, because as discussed in section 2, the carbonate reaction kinetics are too sluggish. To address this, we conducted depressurization experiments and bulk gas analysis via mass spectrometry on aqueous salt solutions equilibrated with air, and lab-grown halite that precipitated under controlled pCO₂ atmospheres (450 ppm, 3000 ppm, and 5000 ppm).

2. Theoretical considerations

We can calculate how much [HCO₃⁻] and [CO₃²⁻] transform into CO₂ before inclusion fluid vaporization. If the measured CO₂ content represents the complete exsolution of TDIC, then previous studies have overestimated and misinterpreted their results (Blamey et al., 2016; Brand et al., 2021, 2016).

The kinetics of the carbonate system equilibrium is essential for understanding the above scenario and is controlled by the following reactions (Kern, 1960):



In reaction (Eq. 1a), gaseous CO_2 is dissolved in water, and hydrolyzes to carbonic acid (Eq. 1b). Hydrogen ions dissociate from carbonic acid to form a bicarbonate ion (Eq. 1c), and further dissociation forms a carbonate ion (Eq. 1d).

The third reaction (Eq. 1c) is considered “instantaneous” (Kern, 1960), and it is impossible to determine whether the hydration reaction occurs directly through the second (Eq. 1b) and third (Eq. 1c) reaction or via the fifth reaction (Eq. 1e) (Eigen et al., 1961). The fifth reaction (Eq. 1e) is sluggish, making it the rate limiting reaction in low pH (<8.2) solutions; however, the sixth reaction (Eq. 1f) is favored at a high pH (>8.2) (Kern, 1960; Johnson, 1982; Dreybrodt et al., 1996). In table 1, k_{+1} to k_{+6} and k_{-1} to k_{-6} are, respectively, the forward and reverse reaction rate constants for the six reactions (Eq. 1a-f).

Assuming the reactions (Eq. 1a and e) are being driven to the left by depressurization, we can calculate the concentration of each species of interest (i.e., $[\text{CO}_2]_{\text{aq}}$ and $[\text{HCO}_3^-]$) that will exsolve before fluid vaporization under high vacuum (10^{-7} to 10^{-8} mbar). Based on our observations from the low-vacuum depressurization experiments in this study, complete fluid vaporization during decrepitation is 5 milliseconds ($0.0004 \text{ L} \cdot \text{s}^{-1}$) (Data availability video). For the reverse reaction of Eq. 1a, the rate is given as:

$$-\frac{\partial[\text{CO}_2]_{\text{aq}}}{\partial t} = k_{-1} \cdot [\text{CO}_2]_{\text{aq}} \quad (\text{Eq. 2a})$$

Where $-\partial[\text{CO}_2]_{\text{aq}}/\partial t$ is the rate in $\text{M} \cdot \text{s}^{-1}$ and k_{-1} is the reverse kinetic rate constant for Eq. 1a (Table 1). Eq. 2a can be integrated to determine the $[\text{CO}_2]_{\text{aq}}$ at a given time:

$$[\text{CO}_2]_t = [\text{CO}_2]_0 \cdot e^{-k_{-1} \cdot t} \quad (\text{Eq. 2b})$$

Where $[\text{CO}_2]_t$ is the CO_2 concentration at a given time, $[\text{CO}_2]_0$ is the starting CO_2 concentration, and t is time in seconds. The rate for Eq. 1e is:

$$-\frac{\partial[\text{HCO}_3^-]}{\partial t} = k_{-5} \cdot [\text{HCO}_3^-] \cdot [\text{H}^+] \quad (\text{Eq. 2c})$$

Where $-\partial[\text{HCO}_3^-]/\partial t$ is the rate in $\text{M} \cdot \text{s}^{-1}$ and k_{-5} is the reverse kinetic rate constant for Eq. 1e (Table 1). Eq. 2c can be integrated to determine the $[\text{HCO}_3^-]$ at a given time:

$$[\text{HCO}_3^-]_t = [\text{HCO}_3^-]_0 \cdot e^{-k_{-5} \cdot [\text{H}^+] \cdot t} \quad (\text{Eq. 2d})$$

Where $[\text{HCO}_3^-]_t$ is the bicarbonate concentration at a given time and $[\text{HCO}_3^-]_0$ is the starting bicarbonate concentration. The exsolution of $[\text{CO}_3^{2-}]$ likely contributes a negligible amount to $[\text{CO}_2]_{\text{aq}}$ as $[\text{CO}_3^{2-}]$ requires protonation in two reaction steps (Eq. 1c and 1d) and is subsequently dehydrated (Eq. 1b). The exsolution of $[\text{CO}_3^{2-}]$ can be ignored as the time required for $[\text{CO}_3^{2-}]$ to

exsolve into $[\text{CO}_2]_{\text{aq}}$ exceeds the inclusion fluid vaporization rate. Kinetic constants for this discussion are assumed to be at STP. Pressure effects on the carbonate kinetic rates are poorly constrained, crucial to accurately characterize the depressurization of a carbonate solution, but Eldik and Palmer (1982) and Millero and Berner (1972) suggest that changes in the carbonate system constants are negligible at low pressures (10^{-7} to 10^{-8} mbar). Pressure dependence has been investigated for reaction k_{-2} , showing a negative linear trend, with values indistinguishable between 1000 and 10,000 mbar (Eldik and Palmer, 1982). Moreover, Millero and Berner (1972) show that the carbonate equilibria constants do not change dramatically with decreasing pressure. Therefore, we assume the kinetic constants are similar to those at STP. Using Eq. 2b and 2d, we calculate that 0.0002% of the $[\text{CO}_2]_{\text{aq}}$ would exsolve into $\text{CO}_2(g)$ and 0.0003% of the $[\text{HCO}_3^-]$ would exsolve into $[\text{CO}_2]_{\text{aq}}$, after 5 milliseconds. Under these conditions, it would take 28 minutes for half of the $[\text{CO}_2]_{\text{aq}}$ to degas and 43 minutes for half of the $[\text{HCO}_3^-]$ to exsolve into $[\text{CO}_2]_{\text{aq}}$. Furthermore, the reverse reaction of Eq. 1e is thermodynamically unfavorable, as the forward reaction is spontaneous (Kern 1960). Nonetheless, 0.004% of the $[\text{CO}_2]_{\text{aq}}$ would dissociate into $[\text{HCO}_3^-]$. Therefore, the kinetics of the carbonate system suggest that a negligible amount of $[\text{HCO}_3^-]$ would be exsolved into $[\text{CO}_2]_{\text{aq}}$ during inclusion decrepitation. The remaining $[\text{HCO}_3^-]$ and $[\text{CO}_3^{2-}]$ should rapidly precipitate as a carbonate salt after solution vaporization.

We can estimate how quickly NaHCO_3 precipitates during the decrepitation process by applying classical nucleation theory (Mullin, 2001), which is described as follows:

$$J = A \exp \left(-\frac{1}{\ln(\Omega)^2} \right) \quad (\text{Eq. 3a})$$

Where J is the rate of nucleation, A is the pre-exponential factor (or the frequency of molecular collisions), and Ω is the solution saturation index. In our context, the solution saturation can be written as:

$$\Omega = \frac{[\text{Na}^+][\text{HCO}_3^-]}{K_{\text{sp}}(\text{NaHCO}_3)} \quad (\text{Eq. 3b})$$

Where $K_{\text{sp}}(\text{NaHCO}_3)$ is the solubility constant for NaHCO_3 (Drever, 1997). A solution $\Omega > 1$ indicates that the solution is saturated with respect to the products. From Eq. 3a, the rate of nucleation is controlled by the degree of saturation. As saturation increases, the nucleation rate increases rapidly until NaHCO_3 salt precipitates. With the near instantaneous vaporization of the inclusion fluid, the solution becomes supersaturated almost instantaneously, causing the HCO_3^- and CO_3^{2-} to precipitate as a carbonate salt by combining with the dissolved metal cations. Given the rapid vaporization time compared to the slow carbonate equilibrium kinetics, the exsolution of $[\text{HCO}_3^-]$ and $[\text{CO}_3^{2-}]$ would contribute a negligible amount to the measured CO_2 content.

3. Methods

3.1. Preparation of stock solutions

A 0.25 M NaHCO_3 solution and a 3.5 wt% Instant Ocean Sea Salt solution (spectrum brand) were made with Millipore water ($18 \text{ M}\Omega \cdot \text{cm}$) and allowed to equilibrate with laboratory atmosphere. Solution pH, temperature, and overlying pCO_2 were measured prior to experiments on an Oakton pH 150, a ThermoPro TP50 Digital hygrometer and thermometer, and an Aranet4 CO_2 meter, respectively. The Aranet4 CO_2 meter uses a nondispersive infrared sensor to measure the concentration of CO_2 . The 3.5 wt% Instant Ocean Sea Salt solution was used to replicate

modern ocean water conditions as it is an excellent comparison (Pretet et al., 2014). The carbonate species were calculated using the carbonate open system equations (Drever, 1997).

3.2. Low-vacuum depressurization experiments

To test whether rapid fluid vaporization of a carbonate solution leaves behind the expected mass of carbonate salt and to visually observe complete fluid vaporization, we performed depressurization experiments by placing 2 and 25 microliters of the 0.25 M NaHCO_3 solution inside a microcapsule using a syringe (Hamilton). The microcapsules were filled and placed in a glass vial connected to an ultratorr on a vacuum line, with temperature and pressure measured before the solution was exposed to a vacuum of 10^{-3} mbar (Fig. 1). The glass vial was exposed to vacuum until the solution in the microcapsule evaporated and the pressure stabilized. A video of the experiment being conducted in a capillary tube is available in the data availability section. After the vacuum experiment, the microcapsule was retrieved and weighed on a microbalance to determine the mass of the resulting NaHCO_3 salt. The 25 μL experiments were conducted in the same manner as the 2 μL experiments.

Gravimetric measurements of the stock solution in the microcapsule proved challenging because rapid evaporation of the small volumes of water prevented the microbalance from stabilizing, hindering accurate determinations of the amount of NaHCO_3 in individual experiments necessary for mass balance purposes. Instead, the average mass of the 2 μL and 25 μL stock solutions was determined gravimetrically by using the syringe to repeatedly decant the 2 μL and 25 μL solutions into an enclosed tin capsules to prevent evaporation; the mean of the 2 μL solution from the syringe was $\bar{x} = 1.92$ mg ($2\sigma = 0.23$; $n = 25$) and mean of the 25 μL was $\bar{x} = 25.19$ ($2\sigma = 0.34$; $n = 10$).

3.3. Lab-grown halite crystals

Halite crystals were grown from NaCl (Fisher Science Education Brand: S25541) dissolved in Millipore water ($18 \text{ M}\Omega\cdot\text{cm}$) under three experimental treatment conditions: one under normal laboratory pCO_2 conditions and two under elevated pCO_2 conditions (~ 3000 and ~ 5000 ppmV). Halite precipitated under open lab conditions formed under variable pCO_2 of 774 ± 23 to 384 ± 12 ppm. This batch of halite precipitated under a temperature range of $23 \pm 0.4^\circ\text{C}$ to $26.7 \pm 0.4^\circ\text{C}$. CO_2 was monitored using an Aranet4 CO_2 meter. Additionally, halite crystals were grown under normal laboratory conditions with a 0.01 M NaHCO_3 solution added to the NaCl saturated water. Clean beakers and petri dishes were used to prevent biological material from altering the trapped gas chemistry. Halite precipitation at elevated pCO_2 was achieved by placing NaCl saturated water into a sealed pressure vessel, which is designed to maintain unique atmospheric gas compositions (Ryan et al., In Review) (Fig. 1). The saturated halite solution was then placed inside the pressure vessel, sealed, and then purged with ‘zero’ grade dry air (Airgas) to remove the humidity and reduce the CO_2 concentration to near zero (Appendix Fig. S1). Following purging, 1000 mbar of zero grade air was injected into the pressure vessel to simulate the modern major atmospheric gas composition, as it is comparable ($78.5 \pm 2\%$ N_2 , $21.5 \pm 2\%$ O_2 , balanced Ar; Airgas, Radon, PA, USA), minus humidity and CO_2 . The CO_2 content was controlled by injecting medical grade CO_2 (Airgas) into the pressure vessel using a low-pressure regulator. CO_2 levels were monitored using the Aranet4 CO_2 meter placed inside the pressure vessel (Fig. 1). Two batches of halite crystals were precipitated under two elevated pCO_2 conditions. The first batch precipitated over a few days under a maximum pCO_2 of 3568 ± 107 and a minimum pCO_2 of 3020 ± 91 ppm, and a temperature range of $17.6 \pm 0.4^\circ\text{C}$ to $20.1 \pm 0.4^\circ\text{C}$. The second batch

precipitated under a maximum $p\text{CO}_2$ of 5329 ± 160 and a minimum 4705 ± 141 ppm at temperature range of $18.5 \pm 0.4^\circ\text{C}$ to $20.6 \pm 0.4^\circ\text{C}$. During halite precipitation, pressure and humidity were also monitored using the Aranet4 CO_2 meter (Appendix Fig. S2). Auxiliary cations and anions are likely present in the halite samples but unaccounted for, as the dominant effect on gas solubility is from the sodium and chlorine ions (Hermann et al., 1995). The resulting halite crystals entrapped both primary gaseous and aqueous fluids inside their inclusions.

3.4. Measuring volatile contents from fluid inclusions in halite and stock solutions by mass spectrometry

Following the methods of Pettitt and Schaller (2020) and Park and Schaller (2025), 60 to 120 milligrams of lab-grown halite was loaded into a custom inlet, and mechanically decrepitated to release the trapped gaseous and aqueous volatiles directly into a Pfeiffer Prisma Plus 1-100 amu quadrupole mass spectrometer (QMS). Adsorbed gases were removed from the samples by pumping them to a high vacuum (10^{-7} to 10^{-8} mbar). 0.2 microliters of 3.5 wt% Instant Ocean salt and 0.25 M NaHCO_3 solutions were loaded into a calibrated pipet volume using a syringe (Hamilton). The solution volume fully occupied the pipet to achieve a minimal amount of headspace. To isolate the solutions from the high vacuum inlet, a cobalt alloy ball stem tip (Swagelok) is compressed onto the mating surface of the volume pipet, forming a gas-tight seal (Pettitt and Schaller, 2020) (Fig. 1). Solutions encapsulated in the pipettes were loaded into the custom inlet, evacuated to high vacuum, and rapidly depressurized, releasing the volatiles through a water trap and directly into the QMS. Similarly, halite samples were crushed into the inlet and through the water trap into the QMS. Upon introduction to the QMS, volatiles produce transient peaks in ion current on a secondary electron multiplier. The quadrupole is tuned to monitor the ion current at m/z 14, 15, 16, 18, 28, 32, 40, and 44 with a 50 millisecond dwell time at each nominal mass. M/z 14 is used to quantify N_2^+ because a mass interference from CO^+ exists at m/z 28 (Graney and Kesler, 1995; Pettitt and Schaller, 2020). A separate interference from CH_4^+ occurs at m/z 14 but is subtracted after calculating the fragmentation from m/z 15 and 16 from a separate methane calibration. H_2O^+ , O_2^+ , Ar^+ , and CO_2^+ were measured at m/z 18, 32, 40, and 44, respectively. A cold cathode ion gauge was used in tandem with the QMS experiments and a transient rise in pressure is observed along with the ion current peaks. The pressure measurement is used as a metric for total gas released from each crush. Pettitt and Schaller (2020) show that there is no observable effect of the cold cathode gauge on the measured gas composition as the gauge is active during both calibration and sample analyses.

The integrated area of the ion current peak for each species is compared to a calibration curve generated from a calibrated gas mixture and used to quantify the total moles of each gas in the unknown samples. For more details about the instrument setup, calibration method, and measured gas composition errors and reproducibility, consult Pettitt and Schaller (2020), Pettitt et al. (2020), and Park and Schaller (2025). A dry air standard of $78.18 \pm 1.56\%$ N_2 , $20.84 \pm 0.42\%$ O_2 , $0.938 \pm 0.019\%$ Ar , and 391.1 ± 7.8 ppm CO_2 made by Airgas (Radnor, PA, USA) is used to calibrate the instrument. Calibration curves are made from the controlled release of known amounts of standard using calibrated pipette volumes filled at measured pressures and temperatures (Pettitt and Schaller, 2020). This method of calibration mimics the burst of gas from crushing inclusions and enables quantification down to the femtomol level.

3.5. Gas-aqueous partitioning of volatiles

The gas phase in the experimental stock solutions corresponds to the headspace when the volume pipet is sealed off with the stem tip (Fig. 1), whereas the aqueous phase is comprised of the dissolved atmospheric gases at equilibrium with the atmosphere at the time of isolation. For inclusions in the lab-grown halite, the gas phase corresponds to the atmosphere under which the halite precipitated, whereas the aqueous phase are the atmospheric gases dissolved at equilibrium. The total moles released from the depressurization and decrepitation experiments represent a spectrum of compositions bounded by the fully gaseous and fully aqueous endmembers. Thus, the gas and aqueous composition must be partitioned to determine the true composition of the atmosphere under which the stock solution and lab-grown halite equilibrated. This gas-aqueous partitioning procedure (MAGPI: Method for Atmospheric Gas Partitioning from fluid Inclusions) is briefly described below, but consult Park and Schaller (2025) for details on the method development, source code, assumptions, and measurement reproducibility and errors. Partitioning the gas phase from the aqueous phase is based on the measured gas ratios (N_2/Ar). The gas ratios can be used to partition the contributions from both the gaseous and aqueous phases to obtain the true atmospheric composition by using:

$$X_j^{atm} = \frac{n_j^{obs}}{\left(\frac{\phi_g}{RT} + (1-\phi_g)H_s^i(T,S)\right)} \left[\sum_{i=1}^M \frac{n_i^{obs}}{\left(\frac{\phi_g}{RT} + (1-\phi_g)H_s^i(T,S)\right)} \right]^{-1} \quad (\text{Eq. 4})$$

Where X_j^{atm} is the mole fraction of the atmospheric component of the volatile of interest; n_j^{obs} is the moles observed of the volatile of interest; M are the volatiles taken into consideration (N_2 , O_2 , Ar , and CO_2); n_i^{obs} is the total moles observed of the analysis; ϕ_g is the gas volume fraction calculated from the N_2/Ar ratio; R is the universal gas constant; T is the temperature of the fluid inclusion in Kelvin; H_s^i is the temperature and salinity dependent Henry's solubility constant of the gas of interest; and S is the salinity of the fluid inclusion. The solubility of each gas is dependent on the temperature and the salinity of the brine (Onda et al., 1970; Hermann et al., 1995). MAGPI was used to perform the calculations on all the decrepitation and depressurization data present in this study. Our measured gas contents are reported with uncertainties at the 95% confidence interval. Errors are propagated using standard techniques following Ku (1996).

3.6. Raman spectroscopy

Raman spectroscopy is employed to meet several objectives: 1. To test whether the residue from the low-vacuum depressurization experiment is $NaHCO_3$ salt; 2. To determine inclusion salinity so that an accurate Henry's solubility constant is used for calculating the gas volume fraction; and 3. To further validate that the fluid inclusions in lab-grown halite capture the overlying atmosphere during precipitation by analyzing gas dominated inclusions. Salinity calibration and inclusion analysis were performed on a Horiba XploRA confocal Raman spectrometer at Rensselaer Polytechnic Institute (RPI) following the calibration technique of Sun et al. (2010), described below. Analysis of the experimental residue was performed on a Bruker Senterra Raman spectrometer at RPI. Measurements on both instruments use a 532 nm green laser at 20 mW power. Using a 600-diffraction grating, measurements were made with a 50x objective and a 50 μm aperture at 2 cm^{-1} spectral resolution. Experiments were integrated for 30 seconds with 3 accumulations. Analysis of the gas dominated inclusion used a 1200-diffraction grating and was integrated for 300 seconds with 3 accumulations. Raman spectra were exported to OriginPro graphing and analysis software and background corrected.

We performed laser Raman spectroscopy on the low-vacuum experimental residue to determine whether the residue is in fact NaHCO_3 salt in either the amorphous or the expected crystalline form. NaHCO_3 has four main active Raman bands, where weak bands occur at 688 cm^{-1} (ν_4 , in-plane deformation) and 1432 cm^{-1} (ν_3 , C–O antisymmetric stretch), a medium strength band at 1271 cm^{-1} (ν_1 , C–O symmetric stretch), a very strong band at 1048 cm^{-1} (ν_1 , C–O symmetric stretch), and eight translational lattice bands between $80\text{--}250\text{ cm}^{-1}$ (Frezzotti et al., 2012). We compared the spectra of the experimental residue to the original NaHCO_3 salt as well as to the glass microcapsule.

Accurate temperature and salinity data are essential for calculating Henry’s solubility constants for each volatile species (N_2 , O_2 , Ar, and CO_2), and are necessary inputs to the gas-aqueous partitioning calculation using MAGPI. The temperatures of the stock solutions and the lab-grown halite were recorded prior to gas analysis of the samples. Stock solution salinity was determined from the added constituents. However, the salinity of the fluid inclusions in halite was quantified through Raman spectroscopy by following the method of Sun et al. (2010), which quantifies $[\text{Cl}^-]$ in the inclusion and can be converted to an equivalent NaCl salinity. Salinity of the NaCl solution was determined via Raman spectroscopy rather than relying on the initial aqueous concentrations because evaporation during halite precipitation increases brine salinity to an unknown value (Lowenstein et al., 2001). The salinity of the trapped brine in the inclusion is the salinity of the brine at the time of precipitation, and determination via Raman spectroscopy is a reliable and accurate method to quantify inclusion salinity in the lab-grown halite (He et al., 2024; Sun, 2009; Sun et al., 2010). $[\text{Cl}^-]$ was estimated by deconvoluting the OH^- stretch of H_2O into two peaks at 3220 cm^{-1} and at 3450 cm^{-1} . The relative intensity changes between the two deconvoluted peaks relative to pure water is used to estimate $[\text{Cl}^-]$ in the inclusion. Deconvolution was performed in the OriginPro graphing and analysis software. The average salinity of the lab-grown halite is $\sim 39\text{ wt}\%$ ($\sim 6.7\text{ mol/L}$ of NaCl) (Appendix Fig. S3).

We further validate the assertion that inclusions in halite trap samples of atmospheric gases during mineral formation by *in-situ* analysis of a gas-dominated inclusion using laser Raman spectroscopy. This was accomplished by comparing the atmospheric N_2/O_2 ratio under which the lab-grown halite precipitated to the N_2/O_2 intensity ratio of the gas trapped within the inclusion. Such a comparison is possible because Raman intensity is proportional to the number of molecules present (Pelletier, 1999), allowing for accurate assessment of the gas composition trapped within the inclusion. N_2 has one strong active Raman band at 2331 cm^{-1} ($\text{N}\equiv\text{N}$ stretch) and O_2 has one strong active Raman band at 1555 cm^{-1} ($\text{O}=\text{O}$ stretch) (Burke, 2001; Frezzotti et al., 2012). Further comparisons were made between the measured N_2/O_2 values from the bulk gas analyses and the N_2/O_2 intensity ratios obtained by the Raman spectrometer. Both the Raman spectra and the gas analyses are expected to reflect the injected N_2/O_2 ratio of 3.73 ± 0.2 , a value similar to the modern atmosphere (Brimblecombe, 1996). The birefringence of the halite should not affect the quantification of N_2 and O_2 , as halite is isotropic and does not influence the Raman peak intensities of interest (Caumon et al., 2015; Hudgins et al., 2024). Furthermore, a confocal Raman spectrometer was used, which bypasses the halite crystal ensuring that it does not contribute to the analysis (Fries and Steele, 2011).

4. Results

4.1. Low-vacuum depressurization experiments of a carbonate solution

Masses of the residues resulting from the low-vacuum depressurization experiments fall on the 1:1 line for both the 2 μL ($\bar{x} = 0.043 \text{ mg}$; $\sigma = 0.003$; $n = 10$) and 25 μL ($\bar{x} = 0.523 \text{ mg}$; $\sigma = 0.009$; $n = 2$) volumes, and are within the expected syringe-mass procedural error (2 μL ; $0.043 \text{ mg} \pm 0.003$, and 25 μL ; $0.525 \text{ mg} \pm 0.014$) (Fig. 2 and Table 2). Our experimental results do not noticeably deviate from the expected yields based on calculations in section 3.2, suggesting that the majority of HCO_3^- and CO_3^{2-} does not transform into CO_2 . Although, the amount of CO_2 released could not be quantified as the equipment used did not have enough significant figures to accurately quantify the expected CO_2 loss gravimetrically. However, CO_2 was quantified for the depressurization and decrepitation experiments performed on the QMS.

Peaks in the Raman spectra of the experimental residue match those in the spectrum of the original NaHCO_3 salt (Fig. 3), confirming that the residue is the original carbonate salt (and is distinct from glass microcapsule). The main Raman bands are observed at 688 cm^{-1} , 1048 cm^{-1} , and 1271 cm^{-1} , matching those of NaHCO_3 (Frezzotti et al., 2012). Additional Raman bands occur at 1017 cm^{-1} and 1064 cm^{-1} corresponding to HCO_3^- and CO_3^{2-} , respectively (Davis and Oliver, 1972). However, the weaker HCO_3^- band at 1360 cm^{-1} is not present within the residue spectra (Frezzotti et al., 2012). The residue's translational lattice band structure is consistent with that of NaHCO_3 , indicating that the residue is crystalline. However, the broadening of the spectral bands at 1048 cm^{-1} and within the translational lattice range at 228 cm^{-1} , 205 cm^{-1} , 166 cm^{-1} , 153 cm^{-1} , 145 cm^{-1} , 114 cm^{-1} , and 92 cm^{-1} suggest that some of the residue is amorphous. A partly amorphous structure of the experimental residue is likely a consequence of rapid NaHCO_3 precipitation during solution vaporization, and therefore consistent with our initial hypothesis.

4.2. Quadrupole mass spectrometry depressurization and decrepitation experiments

Quadrupole mass spectrometry was used to quantify the abundance of the major atmospheric gases on the stock solutions and lab-grown halite, and we observe mole fractions that lie between the air and air-saturated brine (ASB) endmembers with varied gas volume fractions (Appendix Fig. S4). The measured CO_2 mol percent (mol%) and CO_2 normalized to argon (CO_2/Ar) were both compared to expected values calculated using the gas volume fraction (ϕ_g), aqueous solubility of each gas, and temperature and salinity of the solution. ϕ_g was obtained from the measured N_2/Ar ratios as described in section 3.5. At a given ϕ_g and assuming that the gas content solely originates from an air-ASB mixture, the expected molar abundance of each gas of interest is calculated using the following equation:

$$n_j^{\text{calc}} = P n_j * \left[(H_n(T, S) + \phi_g) \left(\frac{1}{RT} - H_n(T, S) \right) \right] \quad (\text{Eq. 5})$$

From the calculated expected molar abundance, an expected CO_2 mol% and CO_2/Ar for a given gas volume fraction can be estimated, allowing for comparisons with the measured CO_2 content. Where n_j^{calc} is the number of mols for each gas of interest; $P n_j$ is the partial pressure of the gas of interest where $p\text{N}_2$, $p\text{O}_2$, $p\text{Ar}$ was set to 0.7808, 0.2095, and 0.093, while $p\text{CO}_2$ was adjusted to the measured $p\text{CO}_2$ values from the Aranet4. Solubility constants were adjusted to the measured temperature and salinity values. The measured vs expected $\text{CO}_2\%$ and CO_2/Ar show a linear relationship that closely aligns with the 1:1 slope corresponding to CO_2 derived solely from an air-ASB mixture (Fig. 4 and consult Table 3 for regression equations). We statistically evaluate whether the measured versus expected averages and slopes deviate from the 1:1 using both analysis of variance (ANOVA) and analysis of covariance (ANCOVA) tests. ANOVA compares the averages of two or more groups by analyzing variance, while ANCOVA compares

the regression slopes of two or more groups by analyzing the means of the dependent variable (McDonald, 2014). The averages and slopes of the measured CO₂% and CO₂/Ar are statistically indistinguishable from the 1:1 line (Fig. 4 and consult Table 3 for statistics). However, there is a statistically significant deviation of the CO₂/Ar slope from the slope of the 1:1 line based on the ANCOVA test ($F=4.72$; $p(\alpha)=0.04$). This deviation may be due to the argon normalization slightly shifting the slope from the 1:1 line. However, the confidence interval for the CO₂/Ar slope overlaps with the 1:1 line (Fig. 4).

Using equation 4, a unique correction was applied to each of the stock solutions and lab-grown halite analyses (Park and Schaller, 2025). The raw data was partitioned into their gaseous and aqueous endmembers to determine the atmospheric composition that each equilibrated under. When partitioned, the N₂, O₂, and Ar converge on values that are indistinguishable from the modern atmosphere and the atmosphere used inside the pressure vessel (Appendix Fig. S5). The partitioned CO₂ from the lab-grown halite that precipitated under “normal” and elevated pCO₂ fall within the expected pCO₂ range of their respective conditions (Fig. 5 and Table 4). Because laboratory pCO₂ is variable, the pCO₂ with which the stock solutions had equilibrated was recorded before the setup of each depressurization experiment. The partitioned CO₂ from the stock solutions falls along the expected 1:1 line corresponding to pCO₂ measured by the Aranet4. CO₂% and CO₂/Ar of the unpartitioned and partitioned gases from the stock solutions and lab-grown halite are compared to each other and shown in Fig. 6 and values are in Table 5.

4.3. Depressurization and total dissolved inorganic carbon

To test whether the measured CO₂ solely represents air-ASB CO₂ or the exsolution of TDIC, we modeled the expected CO₂ content for both end-member scenarios over a range of gas volume fractions (ϕ_g). The modeled CO₂% and CO₂/Ar for an air-ASB mixture were calculated using equation 5. In contrast, the complete TDIC exsolution model was generated by estimating TDIC from the measured pH, pCO₂, temperature, and salinity of each solution, using the open carbonate system equations (Drever, 1997). For this model, we assumed that the TDIC completely exsolved into CO₂ (aq), and the resulting CO₂ (aq) was used with the appropriate Henry’s constant in equation 5. The solubility constants were adjusted to the measured temperature, salinity, and whether the solution was NaCl or NaHCO₃ dominated, producing a unique CO₂ model for each stock solution (Hermann et al., 1995). We then compared the measured CO₂ content from each stock solution to the modeled expectation as a function of ϕ_g (Fig. 7). The measured CO₂% (<1%) and CO₂/Ar (<1) values are consistent with the air-ASB CO₂ model at the measured gas volume fraction range (0.01-0.07). In contrast, the complete exsolution of TDIC model yields CO₂ >84% and >480 CO₂/Ar for the same gas volume fraction range (Fig. 7). TDIC exsolution models were not calculated for the lab-grown halite, as the inclusion pH could not be estimated. Although we attempted to quantify inclusion pH using the Raman method of Hudgins et al. (2024), it was unsuccessful at these concentrations. However, if we assume that the initial pH of the halite solution reflects the inclusion pH, the measured lab-grown halite CO₂ content aligns with the air-ASB CO₂ model for a given ϕ_g (Appendix Fig. S6).

4.4. Raman spectra of a gas dominated lab-grown inclusion

Raman analysis on a gas dominated inclusion shows the main peaks for N₂ and O₂ present at 2331 cm⁻¹ and 1555 cm⁻¹ (Burke, 2001; Frezzotti et al., 2012) (Fig. 8). Ratioed peak intensities of N₂ and O₂ (I_{N2}/I_{O2}) give a value of 3.84 ± 0.2 , which closely aligns with the atmospheric value under which the halite precipitated (3.73 ± 0.2), and is distinct from the aqueous end-member

ratio of 1.73 ± 0.2 . Furthermore, the I_{N_2}/I_{O_2} is in range with the N_2/O_2 content from the lab-grown halite and stock solutions bulk gas analyses ($\bar{x} = 4.12 \pm 0.50$) (Fig. 9). This suggests that direct N_2/O_2 measurements can be obtained prior to the ice core record via Raman spectroscopic methods (Ikeda et al., 1999; Ohno et al., 2021). Future hypothesis testing should focus on measuring N_2/O_2 in natural samples, and test whether N_2 or O_2 is excluded during halite crystallization, similar to the ice core record (Bender, 2002). However, in our analysis, it does not appear that the lab-grown halite excludes N_2 or O_2 during crystallization.

5. Discussion

5.1. CO_2 from inclusion analysis is a mix of air and air-saturated brine

The measured CO_2 from the depressurization and decrepitation experiments are in close agreement with the expected endmembers of air-ASB, and not the complete or even partial exsolution of TDIC (Fig. 4, 6, 7). This is supported by the statistically identical averages and slopes of the expected versus measured CO_2 (Fig. 4 and Table 3), and the large differences between the measured CO_2 content and the complete TDIC exsolution model (Fig. 7). Our data is also consistent with the kinetics of the carbonate system equilibria, showing that equilibrium is too sluggish to allow exsolution of a substantial amount of HCO_3^- or CO_3^{2-} during fluid inclusion decrepitation. During fluid vaporization, the $[HCO_3^-]$ and $[CO_3^{2-}]$ become super saturated, causing rapid nucleation of carbonate salts (Mullin, 2001). Therefore, a carbonate salt residue should be observed after both the low-vacuum and QMS depressurization experiments. As shown in section 4.1, the white residue remaining in the microcapsule following the low-vacuum experiments has a Raman spectrum consistent with $NaHCO_3$ salt, and the masses of the salts confirm that a quantitative conversion occurred (Fig. 2 and 3). The mass of the residue around the rim of the volume pipets following the QMS depressurization experiment was not collected, because the volume pipet greatly exceeds the mass limitation of the RPI microbalance. However, the 0.25 M $NaHCO_3$ solution was used in both the low-vacuum and depressurization experiments, and we interpret the white residue around the rim of the volume pipet to be $NaHCO_3$ salt based on the Raman spectra collected from the low-vacuum experiments. Carbonate salt precipitation following boil off of the solution water is supported by experiments on 1 wt% Na_2CO_3 and $NaHCO_3$ solutions (Cui et al., 2001). However, Cui et al. (2001) did not measure the mass of the residue to confirm a quantitative conversion had occurred, and these experiments were conducted at ca. 1 atm, not under vacuum.

Further evidence that the carbonate system equilibria is slower than the rate of carbonate-salt precipitation comes from the equilibration time of a 0.5 M $NaHCO_3$ solution prepared to determine the equilibration time of a carbonate solution to a new atmospheric condition (Fig. 10) (Kern, 1960; Hudgins et al., 2024). Desired weights of $NaHCO_3$ were placed in 50 mL centrifuge tubes and continuously mixed with 50 mL of Millipore water ($18\text{ M}\Omega\cdot\text{cm}$) until fully dissolved. To ensure the solution reached equilibrium with the laboratory atmosphere, the pH was monitored until the values plateaued. The solution reached equilibrium in approximately 3 hours (Fig. 10), suggesting that an inclusion does not have enough time to equilibrate before rapid vaporization.

In the short time between rupturing a fluid inclusion, but before fluid vaporization, partial exsolution of TDIC could occur in principle, and could contribute to the measured CO_2 content, potentially inflating measured CO_2 values. To explore this possibility, we theoretically estimate the magnitude of this contribution to the measured CO_2 content. Within the 5 milliseconds to boil

off the inclusion fluid during decrepitation, 0.0003% of the $[\text{HCO}_3^-]$ would be converted to $[\text{CO}_2]_{\text{aq}}$ via the reverse reaction of Eq. 1e (Kern, 1960). Although, the reverse reaction of Eq. 1e is thermodynamically unfavorable (Drever, 1997), 0.004% of $[\text{CO}_2]_{\text{aq}}$ would contribute to $[\text{HCO}_3^-]$ via the forward reaction. These contributions are exceedingly small compared to the relative error of the CO_2 measurements in our analysis, which was determined from the 95% confidence intervals ($\bar{x} = 7.1\%$; $\sigma = 4.7\%$). Therefore, the potential contribution of partial TDIC exsolution to the measured CO_2 content is indistinguishable from the instrument uncertainty and does not merit correction.

Uncertainty on the measured CO_2 content and minor deviations from the 1:1 line (Fig. 4) cannot be explained by partial DIC exsolution but may be due to limitations of the analytical technique. The CO_2 content is often quantified close to its femtomol limit of detection, which may account for some of the variation between the expected versus measured (Pettitt and Schaller, 2020). Furthermore, CO_2 is the most soluble of the atmospheric gases, with the largest proportional difference between the gaseous and aqueous phases, where any small change to the ϕ_g has the greatest effect on CO_2 (Park and Schaller, 2025). Another contributing factor to the error and deviation of CO_2 is likely the variability of the $p\text{CO}_2$ levels measured by the Aranet4, as the associated error of the $p\text{CO}_2$ increases with higher partial pressure ($0\text{-}2000 \text{ ppm} \pm 3\%$ and $2001\text{-}9999 \pm 10\%$).

Prior to gas-aqueous partitioning, the measured CO_2 content of the lab-grown halite and stock solutions fall between the expected endmembers of an air-ASB mixture (Fig. 4). However, because CO_2 is highly soluble, interpreting unpartitioned CO_2 from multiphase inclusions as the atmospheric condition will lead to erroneous conclusions. For example, the unpartitioned CO_2 content of halite grown at $\sim 3000 \text{ ppm}$ could be interpreted as having an average $p\text{CO}_2$ of $121,307 \pm 67,298 \text{ ppm}$ (Table 4). In contrast, partitioning the same data yields an average $p\text{CO}_2$ of $3077 \pm 232 \text{ ppm}$, which closely matches the measured $p\text{CO}_2$ the halite precipitated under (Fig. 5 and Table 4). This trend is consistent in the measured CO_2 content, as well as the other gaseous species, in the lab-grown halite and stock solutions (Fig. 5 and 6, Table 4, and Appendix Fig. S5). These findings reinforce that gas-aqueous partitioning is an essential step in inclusion gas analyses to accurately reconstruct the atmospheric condition.

5.2. Biological influences on fluid inclusions in halite

The variability within our data could also be caused by biological processes (e.g., photosynthesis and respiration) altering the O_2 and CO_2 gas chemistry of the fluids trapped within the inclusions, driving them away from the expected equilibrium with atmospheric gas. Complex organic molecules and living microorganisms have been observed in fluid inclusions (Vreeland et al., 2000; Mißbach et al., 2021; Schreder-Gomes et al., 2022). Although this is a far greater concern on natural samples, it is possible that microorganisms and organic matter could have been trapped in fluid inclusions during precipitation of the lab-grown halite, altering the gas chemistry. Despite methodological efforts to avoid this, Raman spectroscopy can verify the presence or absence of trapped organic matter or microorganisms. Raman spectra of fluid inclusions from the lab-grown halite do not show peaks associated with organic molecules (Appendix Fig. S7) (Fries and Steele, 2011; Lu et al., 2011). However, it is possible that organic matter or microbes were not detected by the Raman spectrometer may occur due to the analyte of interest being below the limit of detection. An additional test to determine biological influence on the lab-grown halite data follows the method of Park and Schaller (2025). To determine if the O_2 and CO_2 measured is influenced by the expected stoichiometric exchange due to

photosynthesis or respiration, the expected molar abundance of each gas is calculated relative to the observed moles of N₂ and compared to what is observed. The difference between the two can be calculated through the gas-aqueous partition:

$$\Delta n_j = n_j^{obs} - \left(\frac{X_j^{atm}}{X_{N_2}^{atm}} * n_{N_2}^{obs} \frac{\left(\frac{\varphi_g}{RT} + (1-\varphi_g)H_s(T,S) \right)_j}{\left(\frac{\varphi_g}{RT} + (1-\varphi_g)H_s(T,S) \right)_{N_2}} \right) \quad (\text{eq. 6})$$

Where j is the gas of interest, the X_j/X_{N₂} term is set to reflect the ratios of the modern atmosphere. Excesses and deficits of O₂ and CO₂ can be compared by plotting the ΔO₂ and ΔCO₂. A 1:1 inverse relationship between the data would suggest photosynthesis or respiration altered the gases. However, there are no clear trends observed, suggesting that the observed gas data has not been influenced by photosynthesis or respiration (Fig. 11).

5.3. Inclusions in halite capture a ‘snapshot’ of the atmosphere

By analyzing air bubbles trapped in glacial ice, the Antarctic ice core record has provided direct compositional measurements of the atmosphere of the last 800 Ka with some isolated intervals dating back to 2 million years (Lüthi et al., 2008; Higgins et al., 2015; Yan et al., 2019). Prior to the ice core record, reconstructing Earth’s ancient atmospheric composition has relied on models and a variety of proxy methods that often disagreed in overall trends and absolute values for pCO₂ (CenCO2PIP, 2023). However, as shown by this study and Park and Schaller (2025), inclusions in lab-grown halite clearly trap atmospheric gases during mineral precipitation, where the halite precipitated under controlled atmospheric conditions align with gas compositions introduced into the growth chamber (Fig. 5) (Appendix Fig. S5). Although, Park and Schaller (2025) grew halite in laboratory conditions, this study better controlled the atmospheric conditions during halite precipitation using a sealed pressure vessel. Notably, the halite that precipitated under different CO₂ conditions show distinct CO₂ separation of their respective atmosphere when partitioned. In addition, Raman spectra of a gas dominated inclusion provides secondary evidence that the inclusions in halite trap the atmosphere during mineral formation and are further corroborated with the partitioned N₂/O₂ gas data (Fig. 7 and 8). Thus, we have shown that not only can CO₂ be directly quantified and partitioned to reflect the true atmosphere during halite formation, but O₂ as well (Appendix Fig. S5). This method has the potential to constrain the evolution of atmospheric O₂ throughout Earth history, as existing models and proxies used to reconstruct ancient pO₂ lack consensus and exhibit notable variability and inconsistencies with one another (Berner, 2009; Glasspool and Scott, 2010; Canfield, 2013; Lyons et al., 2014; Steadman et al., 2020; Zhang et al., 2021; Eguchi et al., 2022).

Bulk gas analysis of inclusions trapped in halite has the potential to extend direct atmospheric compositional (and isotopic) constraints beyond the ice core record (Goldstein, 2001). This approach can be used to test Earth’s degassing history (Cadogan, 1977; Avicé et al., 2018; Guo and Korenaga, 2020), as well as the evolution and interplay between the atmosphere, biosphere, lithosphere, and hydrosphere (Marty et al., 2013; Lyons et al., 2014; Krissansen-Totton et al., 2018; Catling and Zahnle, 2020). Specifically, this approach can test whether continental weathering can be the main control of long term pCO₂ levels (Kent and Muttoni, 2013; Schaller et al., 2015), whether the δ¹³C of mantle derived CO₂ has been consistent or varied throughout Earth history (Des Marais and Moore, 1984; Krissansen-Totton et al., 2021), and the relationship between the global mean temperature and increasing pCO₂ (Caballero and Huber, 2013). Bulk gas analysis of inclusions have the potential to address these unresolved

questions as they are crucial for quantitative long-term global carbon cycle models and future CO₂ projections (Berner et al., 1983; Foster et al., 2017).

Fluid inclusion gas analysis has been applied to Proterozoic and Phanerozoic halite to reconstruct modern and ancient atmospheric compositions (Blamey et al., 2016; Blamey and Brand, 2019; Park and Schaller, 2025; Park et al., In Review). After a robust screening protocol for primary inclusions and partitioning the gas-aqueous endmembers (Park et al, in review), the measured CO₂ and O₂ content align remarkably well with existing models and proxies (Canfield, 2013; Foster et al., 2017; Krissansen-Totton et al., 2018; Zhang et al., 2021). However, only after applying the gas-aqueous partitioning method to Blamey et al's. (2016) and Blamey's and Brand's (2019) data does the CO₂ content produce meaningful results (Park et al., In Review). Further highlighting the necessity of applying the gas-aqueous correction to raw inclusion data (Park and Schaller, 2025). Furthermore, the bulk gas analysis of fluid inclusion was able to obtain direct measurements of the $\delta^{13}\text{C}$ from the CO₂ content of a gas dominated sample from the Mesoproterozoic Sibley halite (Ontario, Canada). Park et al. (In Review) report a $\delta^{13}\text{C}$ of -8.38 ± 0.20 ‰ (VPDB) and after applying the appropriate carbon isotope fractionations during gas-water exchange, this value predicts calcite formation with $\delta^{13}\text{C}$ between -0.2 ‰ and 1.6 ‰ (10 - 30°C), which strongly agree with 1.4 Ga marine carbonates (Krissansen-Totton et al., 2015).

Extending the record of Earth's atmospheric CO₂ content beyond the ice cores has heretofore relied on proxies, where the physical, biological, or geochemical property of a fossil or mineral responds to or records some function of the concentration of CO₂ during formation (Royer, 2014). However, inclusions in halite have the potential to extend the direct CO₂ record beyond the temporally restricted ice cores (Yan et al., 2019), as we have shown that halite trap gases that are representative of the overlying atmosphere under which they precipitated. Furthermore, halite have low diffusivity for H₂ and CO₂ at temperatures below 200°C , indicating that the gases can be retained within the mineral for billions of years (Zimmermann and Moretto, 1996). Although, post-depositional processes will alter the initial inclusion chemistry, robust screening protocols are used to identify and exclude altered samples, such as, petrography, micro-thermometry, and Raman spectroscopy. See Blamey and Brand (2019), Brand et al. (2021), and Park and Schaller (2025) for a detailed review of the screening protocol for primary inclusions in halite. Moreover, bulk gas analysis of inclusions is not limited to halite samples as palustrine cherts, soil carbonates, and soil gypsum have produced mole fractions of atmospheric gas compositions that are in excellent agreement with previous model predictions (Schaller et al., 2017; Pettitt et al., 2020).

6. Conclusions

We test whether the CO₂ content measured from bulk gas analysis in fluid inclusions accurately represents the overlying air at various pCO₂ levels during mineral formation, rather than Pettitt et al's. (2020) assumption that the CO₂ measured represents the complete exsolution of TDIC. We find Pettitt et al's. (2020) assumption to be unsubstantiated. We demonstrate that the CO₂ contents measured in inclusions hosted in halite accurately represents the overlying air at various pCO₂ levels, rather than the complete or partial exsolution of TDIC. Our results show that the measured CO₂ content falls between the expected values of air and air-saturated brine at different CO₂ conditions, and by partitioning gas contributions from each phase, we observe atmospheric pCO₂ values closely matching the conditions under which the lab-grown halite precipitated. These findings demonstrate the ability of halite inclusions to faithfully entrap and preserve atmospheric CO₂ but also the other major atmospheric gases (i.e., N₂, O₂, and Ar),

giving us confidence in applying our methods to new and existing analyses of both natural modern and ancient halite-inclusions. Future work should extend this method to other minerals, such as soil carbonates, soil gypsum, and cherts. Bulk gas analysis of fluid inclusions is a promising method to reliably reconstruct the atmospheric composition beyond the ice core record.

CRedit Authorship Contribution Statement

Michael Naylor Hudgins: Conceptualization, Methodology, Formal Analysis, Investigation, Data Curation, Writing – Original Draft, Visualization. **Justin G. Park:** Investigation, Writing – Review & Editing. **Alex M. Ryan:** Investigation, Writing – Review & Editing. **Jessika Rogers:** Investigation, Writing – Review & Editing. **Morgan F. Schaller:** Conceptualization, Resources, Writing – Review & Editing, Supervision.

Data Availability

All data necessary to evaluate the conclusions of this study are available in _____

Declaration of Competing Interest

The authors declare that they have no known competing financial interests or personal relationships that could have appeared to influence the work reported in this paper.

Acknowledgements

A special thank you to Andy Ridgwell, who brought this criticism to our attention following our presentation at the 2023 AGU meeting, as well as many fruitful discussions with Dan Breecker and Wally Broecker. Thank you to Neha Dhull and Frank Spear for enlightening discussions and to Humberto Terrones for the use of the Raman spectrometer. We are grateful for the support and help from the CESIA and RARE members.

Appendix A. Supplementary Material

The following are the Supplementary Material to this article and available at _____

References

- Avice G., Marty B., Burgess R., Hofmann A., Philippot P., Zahnle K. and Zakharov D. (2018) Evolution of atmospheric xenon and other noble gases inferred from Archean to Paleoproterozoic rocks. *Geochim. Cosmochim. Acta* **232**, 82–100.
- Barker C. E. and Goldstein R. H. (1990) Fluid-inclusion technique for determining maximum temperature in calcite and its comparison to the vitrinite reflectance geothermometer. *Geol.* **18**, 1003–1006.
- Bender M. L. (2002) Orbital tuning chronology for the Vostok climate record supported by trapped gas composition. *EPSL* **204**, 275–289.
- Benison K. C. and Goldstein R. H. (1999) Permian paleoclimate data from fluid inclusions in halite. *Chem. Geol.* **154**, 113–132.
- Berner R. A. (2009) Phanerozoic atmospheric oxygen: New results using the GEOCARBSULF model. *Am. J. Sci.* **309**, 603–606.

685 Berner R. A., Lasaga A. C. and Garrels R. M. (1983) The carbonate-silicate geochemical cycle
686 and its effect on atmospheric carbon dioxide over the past 100 million years. *Am. J. Sci.*
687 **283**, 641–683.

688 Blamey N. J. F. and Brand U. (2019) Atmospheric gas in modern and ancient halite fluid
689 inclusions: A screening protocol. *Gondwana Res.* **69**, 163–176.

690 Blamey N. J. F., Brand U., Parnell J., Spear N., Lécuyer C., Benison K., Meng F. and Ni P.
691 (2016) Paradigm shift in determining Neoproterozoic atmospheric oxygen. *Geol.* **44**,
692 651–654.

693 Blamey N., of Mining N. M. I., Boston P., Rosales-Lagarde L., of Mining N. M. I. and College
694 N. S. (2016) High-resolution signatures of oxygenation and microbiological activity in
695 speleothem fluid inclusions. *Int. J. Speleol.* **45**, 231–241.

696 Bodnar R. J. (2003) *Chapter 4. Introduction to Aqueous-Electrolyte Fluid Inclusions.*, Mineral.
697 Assoc. Canada.

698 Brand U., Davis A. M., Shaver K. K., Blamey N. J. F., Heizler M. and Lécuyer C. (2021)
699 Atmospheric oxygen of the Paleozoic. *Earth Sci. Rev.* **216**, 103560.

700 Brimblecombe P. (1996) *Air Composition and Chemistry.*, Cambridge University Press.

701 Burke E. A. J. (2001) Raman microspectrometry of fluid inclusions. *Lithos* **55**, 139–158.

702 Caballero R. and Huber M. (2013) State-dependent climate sensitivity in past warm climates and
703 its implications for future climate projections. *Proc. Natl. Acad. Sci. U.S.A.* **110**, 14162–
704 14167.

705 Cadogan P. H. (1977) Palaeoatmospheric argon in Rhynie chert. *Nature* **268**, 38–41.

706 Canfield D. (2013) Proterozoic Atmospheric Oxygen. *Treatise on Geochemistry: Second Edition*
707 **6**, 197–216.

708 Catling D. C. and Zahnle K. J. (2020) The Archean atmosphere. *Sci. Adv.* **6**, eaax1420.

709 Caumon M.-C., Tarantola A. and Mosser-Ruck R. (2015) Raman spectra of water in fluid
710 inclusions: I. Effect of host mineral birefringence on salinity measurement. *J. Raman*
711 *Spectrosc.* **46**, 969–976.

712 Cui Q., Chandra S. and McCahan S. (2001) The Effect of Dissolving Gases or Solids in Water
713 Droplets Boiling on a Hot Surface. *J. Heat Transf.* **123**, 719–728.

714 Davis A. R. and Oliver B. G. (1972) A Vibrational-Spectroscopic Study of the Species Present in
715 the CO₂-H₂O System. *J. Solution Chem.* **1**, 11.

716 Des Marais D. J. and Moore J. G. (1984) Carbon and its isotopes in mid-oceanic basaltic glasses.
717 *EPSL* **69**, 43–57.

718 Drever J. I. (1997) *The Geochemistry of Natural Waters: Surface and Groundwater*
719 *Environments.*, Prentice Hall.

720 Dreybrodt W., Lauckner J., Zaihua L., Svensson U. and Buhmann D. (1996) The kinetics of the
721 reaction CO₂ + H₂O → H⁺ + HCO₃⁻ as one of the rate limiting steps for the dissolution of
722 calcite in the system H₂O-CO₂-CaCO₃. *Geochim. Cosmochim. Acta* **60**, 3375.

723 Eguchi J., Diamond C. W. and Lyons T. W. (2022) Proterozoic supercontinent break-up as a
 724 driver for oxygenation events and subsequent carbon isotope excursions. *PNAS Nexus* **1**,
 725 pgac036.

726 Foster G. L., Royer D. L. and Lunt D. J. (2017) Future climate forcing potentially without
 727 precedent in the last 420 million years. *Nat. Commun.* **8**, 14845.

728 Frezzotti M. L., Tecce F. and Casagli A. (2012) Raman spectroscopy for fluid inclusion analysis.
 729 *J. Geochem. Explor.* **112**, 1–20.

730 Fries M. and Steele A. (2011) Raman Spectroscopy and Confocal Raman Imaging in Mineralogy
 731 and Petrography. In *Springer Series in Optical Sciences* pp. 111–135.

732 Glasspool I. J. and Scott A. C. (2010) Phanerozoic concentrations of atmospheric oxygen
 733 reconstructed from sedimentary charcoal. *Nat. Geosci.* **3**, 627–630.

734 Goldstein R. H. (2001) Clues from Fluid Inclusions. *Science* **294**, 1009–1011.

735 Graney J. R. and Kesler S. E. (1995) Factors affecting gas analysis of inclusion fluid by
 736 quadrupole mass spectrometry. *Geochim. Cosmochim. Acta* **59**, 3977–3986.

737 Guo M. and Korenaga J. (2020) Argon constraints on the early growth of felsic continental crust.
 738 *Sci. Adv.* **6**, eaaz6234.

739 He X., Wang W.-Q., Liu Y.-Z. and Sun Q. (2024) Raman Quantitative Measurement on the Cl^-
 740 Molarity of H_2O - NaCl - CO_2 System: Application to Fluid Inclusions. *Minerals* **14**, 1121.

741 Hermann C., Dewes I. and Schumpe A. (1995) The estimation of gas solubilities in salt solutions.
 742 *Chem. Eng. Sci.* **50**, 1673–1675.

743 Higgins J. A., Kurbatov A. V., Spaulding N. E., Brook E., Introne D. S., Chimiak L. M., Yan Y.,
 744 Mayewski P. A. and Bender M. L. (2015) Atmospheric composition 1 million years ago
 745 from blue ice in the Allan Hills, Antarctica. *Proc. Natl. Acad. Sci.* **112**, 6887–6891.

746 Hudgins M. N., Ikeda M., Olsen P. E. and Schaller M. F. (2023) Direct measurements of CO_2
 747 from bedded cherts (Inuyama, Japan) supports a link between CAMP volcanism and deep
 748 ocean acidification during the end-Triassic extinction. *AGU Abstract*.

749 Hudgins M. N., Knobbe T. K., Hubbard J., Steele A., Park J. G. and Schaller M. F. (2024) In situ
 750 quantification of carbonate species concentrations, pH, and pCO_2 in calcite fluid
 751 inclusions using confocal Raman spectroscopy. *Appl. Spectrosc.* 00037028241275192.

752 Ikeda T., Fukazawa H., Mae S., Pepin L., Duval P., Champagnon B., Lipenkov V. Ya. and
 753 Hondoh T. (1999) Extreme fractionation of gases caused by formation of clathrate
 754 hydrates in Vostok Antarctic Ice. *Geophys. Res. Lett.* **26**, 91–94.

755 Johnson K. S. (1982) Carbon dioxide hydration and dehydration kinetics in seawater. *Limnol.*
 756 *Oceanogr.* **27**, 849–855.

757 Judd E. J., Tierney J. E., Lunt D. J., Montañez I. P., Huber B. T., Wing S. L. and Valdes P. J.
 758 (2024) A 485-million-year history of Earth's surface temperature. *Science* **385**, eadk3705.

759 Kent D. V. and Muttoni G. (2013) Modulation of Late Cretaceous and Cenozoic climate by
 760 variable drawdown of atmospheric pCO_2 from weathering of basaltic provinces on
 761 continents drifting through the equatorial humid belt. *Clim. Past* **9**, 525–546.

762 Kern D. M. (1960) The hydration of carbon dioxide. *J. Chem. Educ.* **37**, 14.

763 Knobbe T. K. and Schaller M. F. (2018) A tight coupling between atmospheric pCO₂ and sea-
764 surface temperature in the Late Triassic. *Geol.* **46**, 43–46.

765 Krissansen-Totton J., Arney G. N. and Catling D. C. (2018) Constraining the climate and ocean
766 pH of the early Earth with a geological carbon cycle model. *Proc. Natl. Acad. Sci. U.S.A.*
767 **115**, 4105–4110.

768 Krissansen-Totton J., Buick R. and Catling D. C. (2015) A statistical analysis of the carbon
769 isotope record from the Archean to Phanerozoic and implications for the rise of oxygen.
770 *Am. J. Sci.* **315**, 275–316.

771 Krissansen-Totton J., Kipp M. A. and Catling D. C. (2021) Carbon cycle inverse modeling
772 suggests large changes in fractional organic burial are consistent with the carbon isotope
773 record and may have contributed to the rise of oxygen. *Geobiology* **19**, 342–363.

774 Ku H. H. (1996) Notes on the use of propagation of error formulas. *J. Res. Natl. Bur. Stand.* **70**,
775 263–273.

776 Lowenstein T. K., Timofeeff M. N., Brennan S. T., Hardie L. A. and Demicco R. V. (2001)
777 Oscillations in Phanerozoic Seawater Chemistry: Evidence from Fluid Inclusions.
778 *Science* **294**, 1086–1088.

779 Lu X., Al-Qadiri H. M., Lin M. and Rasco B. A. (2011) Application of Mid-infrared and Raman
780 Spectroscopy to the Study of Bacteria. *Food Bioprocess Technol.* **4**, 919–935.

781 Lüthi D., Le Floch M., Bereiter B., Blunier T., Barnola J.-M., Siegenthaler U., Raynaud D.,
782 Jouzel J., Fischer H., Kawamura K. and Stocker T. F. (2008) High-resolution carbon
783 dioxide concentration record 650,000–800,000 years before present. *Nature* **453**, 379–
784 382.

785 Lyons T. W., Reinhard C. T. and Planavsky N. J. (2014) The rise of oxygen in Earth’s early ocean
786 and atmosphere. *Nature* **506**, 307–315.

787 Marty B., Zimmermann L., Pujol M., Burgess R. and Philippot P. (2013) Nitrogen Isotopic
788 Composition and Density of the Archean Atmosphere. *Science* **342**, 101–104.

789 McDonald J. H. (2014) *Handbook of biological statistics.*, Sparky House Publishing.

790 McElwain J. C., Beerling D. J. and Woodward F. I. (1999) Fossil Plants and Global Warming at
791 the Triassic-Jurassic Boundary. *Science* **285**, 1386–1390.

792 McSween H. Y., Richardson S. M. and Uhle M. E. (2003) *Geochemistry: Pathways and*
793 *Processes*. 2nd ed., Columbia University Press.

794 Mills B. J. W., Krause A. J., Jarvis I. and Cramer B. D. (2023) Evolution of Atmospheric O₂
795 Through the Phanerozoic, Revisited. *Annu. Rev. Earth Planet Sci.* **51**, 253–276.

796 Mißbach H., Duda J.-P., van den Kerkhof A. M., Lüders V., Pack A., Reitner J. and Thiel V.
797 (2021) Ingredients for microbial life preserved in 3.5 billion-year-old fluid inclusions.
798 *Nat. Commun.* **12**, 1101.

799 Mullin J. W. (2001) *Crystallization.*, Elsevier Science & Technology, Chantilly, United
800 Kingdom.

801 Norman D. I., Blamey N. J. F. (2001) Quantitative analysis of fluid inclusion volatiles by a
802 quadrupole mass spectrometer system. *ECROFI* **16**, 341–344.

803 Ohno H., Iizuka Y. and Fujita S. (2021) Pure rotational Raman spectroscopy applied to N₂/O₂
804 analysis of air bubbles in polar firn. *J. Glaciol.* **67**, 903–908.

805 Onda K., Sada E., Kobayashi T., Kito S. and Ito K. (1970) Salting-out parameters of gas
806 solubility in aqueous salt solutions. *J. Chem. Eng. Japan* **3**, 18–24.

807 Park J. G., Hudgins M. N., Fralick P., Shelley J. T. and Schaller M. F. (In Review) Breathing life
808 into the “Boring Billion” through direct constraints on atmospheric O₂ and CO₂. *Proc.*
809 *Natl. Acad. Sci.*

810 Park J. G. and Schaller M. F. (2025) Constraints on Earth’s atmospheric evolution from a gas-
811 aqueous partition of fluid inclusion volatiles. *Gondwana Res.* **139**, 204–215.

812 Pelletier M. J. (1999) *Analytical Applications of Raman Spectroscopy*. 1st edition., Blackwell
813 Publishing, Osney Mead, Oxford ; Malden, MA.

814 Petit J. R., Jouzel J., Raynaud D., Barkov N. I., Barnola J.-M., Basile I., Bender M., Chappellaz
815 J., Davis M., Delaygue G., Delmotte M., Kotlyakov V. M., Legrand M., Lipenkov V. Y.,
816 Lorius C., PÉpin L., Ritz C., Saltzman E. and Stievenard M. (1999) Climate and
817 atmospheric history of the past 420,000 years from the Vostok ice core, Antarctica.
818 *Nature* **399**, 429–436.

819 Pettitt E. A., Cherniak D. J., Schaller M. F. and Watson E. B. (2020) Diffusive retention of
820 carbon and nitrogen in a microcrystalline quartz-dominated chert: Implications for
821 reconstructing Earth’s ancient atmosphere. *Chem. Geol.* **541**, 119572.

822 Pettitt E. A. and Schaller M. F. (2020) A new calibration technique for quantitative gas analyses
823 of fluid inclusions using a quadrupole mass spectrometer. *RCM* **34**.

824 Pretet C., Reynaud S., Ferrier-Pagès C., Gattuso J.-P., Kamber B. S. and Samankassou E. (2014)
825 Effect of salinity on the skeletal chemistry of cultured scleractinian zooxanthellate corals:
826 Cd/Ca ratio as a potential proxy for salinity reconstruction. *Coral Reefs* **33**, 169–180.

827 Royer D. L. (2014) Atmospheric CO₂ and O₂ During the Phanerozoic: Tools, patterns, and
828 impacts. In *Treatise on Geochemistry* Elsevier. pp. 251–267.

829 Ryan A., Pryor S., Park J., Herrero-Perez M. J., Rogers K., Shelley J. and Schaller M. F. (In
830 Review) A novel low-cost laboratory apparatus enabling countertop emulation of the
831 surface conditions of the prebiotic Earth. *Submitted to Astrobiology*.

832 Sano Y. and Pillinger C. T. (1990) Nitrogen isotopes and N₂/Ar ratios in cherts: An attempt to
833 measure time evolution of atmospheric $\delta^{15}\text{N}$ value. *Geochem. J.* **24**, 315–325.

834 Schaller M. F., Pettitt E. and Knobbe T. (2017) A potential new proxy for paleo-atmospheric pO₂
835 from soil carbonate-hosted fluid inclusions applied to pristine Chinle soils from the
836 Petrified Forest 1A core. **2017**, PP44A-05.

837 Schaller M. F., Wright J. D. and Kent D. V. (2015) A 30 Myr record of Late Triassic atmospheric
838 pCO₂ variation reflects a fundamental control of the carbon cycle by changes in
839 continental weathering. *Geol. Soc. Am. Bull.* **127**, 661–671.

- Schaller M. F., Wright J. D. and Kent D. V. (2011) Atmospheric pCO₂ perturbations associated with the Central Atlantic Magmatic Province. *Science* **331**, 1404–1409.
- Schreder-Gomes S. I., Benison K. C. and Bernau J. A. (2022) 830-million-year-old microorganisms in primary fluid inclusions in halite. *Geol.* **50**, 918–922.
- Steadman J. A., Large R. R., Blamey N. J., Mukherjee I., Corkrey R., Danyushevsky L. V., Maslennikov V., Hollings P., Garven G., Brand U. and Lécuyer C. (2020) Evidence for elevated and variable atmospheric oxygen in the Precambrian. *Precambrian Res.* **343**, 105722.
- Sun Q., Zhao L., Li N. and Liu J. (2010) Raman spectroscopic study for the determination of Cl⁻ concentration (molarity scale) in aqueous solutions: Application to fluid inclusions. *Chem. Geol.* **272**, 55–61.
- The Cenozoic CO₂ Proxy Integration Project (CenCO₂PIP) Consortium*†, Hönisch B., Royer D. L., Breecker D. O., et al. (2023) Toward a Cenozoic history of atmospheric CO₂. *Science* **382**, eadi5177.
- Tierney J. E., Poulsen C. J., Montañez I. P., et al. (2020) Past climates inform our future. *Science* **370**, eaay3701.
- Van Eldik R. and Palmer D. A. (1982) Effects of pressure on the kinetics of the dehydration of carbonic acid and the hydrolysis of CO₂ in aqueous solution. *J. Solution Chem.* **11**, 339–346.
- Vreeland R. H., Rosenzweig W. D. and Powers D. W. (2000) Isolation of a 250-million-year-old halotolerant bacterium from a primary salt crystal. *Nature* **407**, 897–900.
- Williams A. E. (1996) Mass spectrometric analysis of volatiles in fluid inclusions: aliquot calibration valve to simulate inclusion rupture. *Chem. Geol.* **131**, 155–165.
- Yan Y., Bender M. L., Brook E. J., Clifford H. M., Kemeny P. C., Kurbatov A. V., Mackay S., Mayewski P. A., Ng J., Severinghaus J. P. and Higgins J. A. (2019) Two-million-year-old snapshots of atmospheric gases from Antarctic ice. *Nature* **574**, 663–666.
- Yeung L. Y. (2017) Low oxygen and argon in the Neoproterozoic atmosphere at 815 Ma. *EPSL* **480**, 66–74.
- Zeebe R. E. and Wolf-Gladrow D. (2001) *CO₂ in Seawater: Equilibrium, Kinetics, Isotopes.*, Gulf Professional Publishing.
- Zhang S., Wang H., Wang X. and Ye Y. (2021) The Mesoproterozoic Oxygenation Event. *Sci. China Earth Sci.* **64**, 2043–2068.
- Zimmermann J. L. and Moretto R. (1996) Release of water and gases from halite crystals. *Eur. J. Mineral.* **8**, 413–422.

879 Figures and Tables

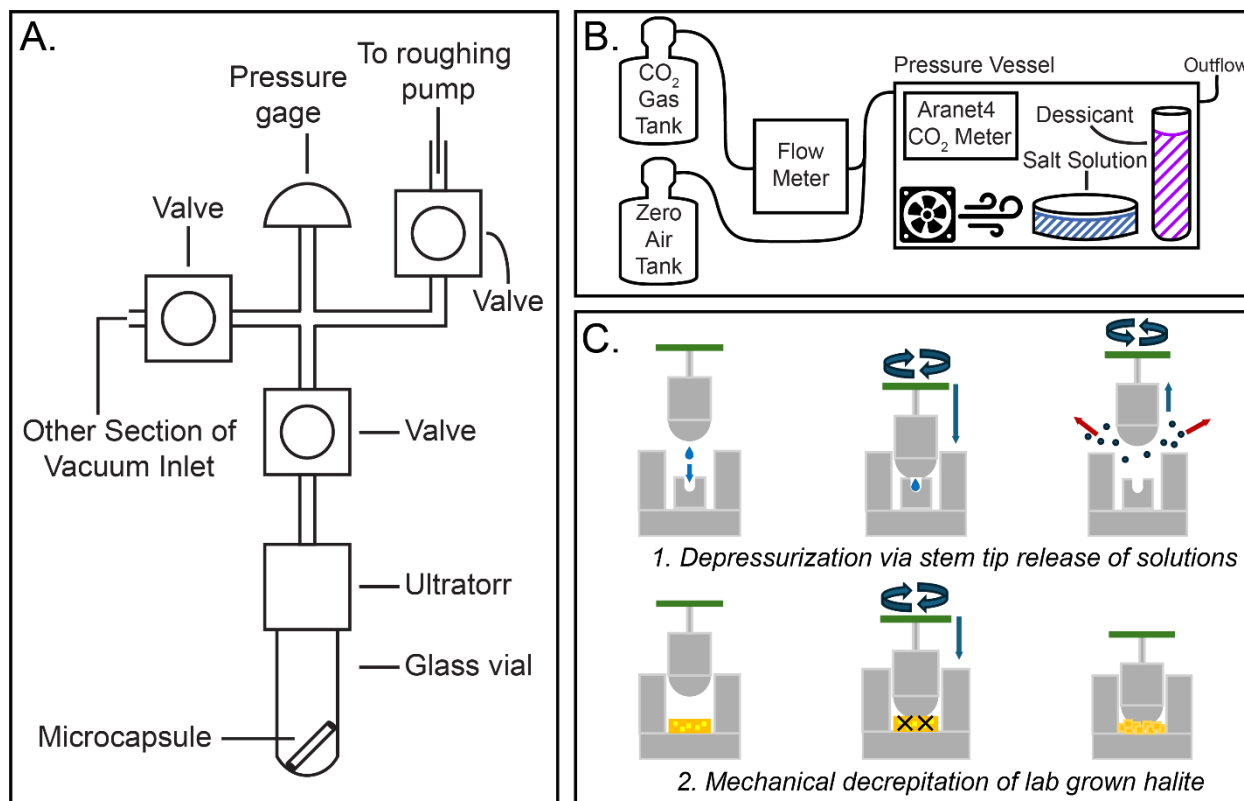
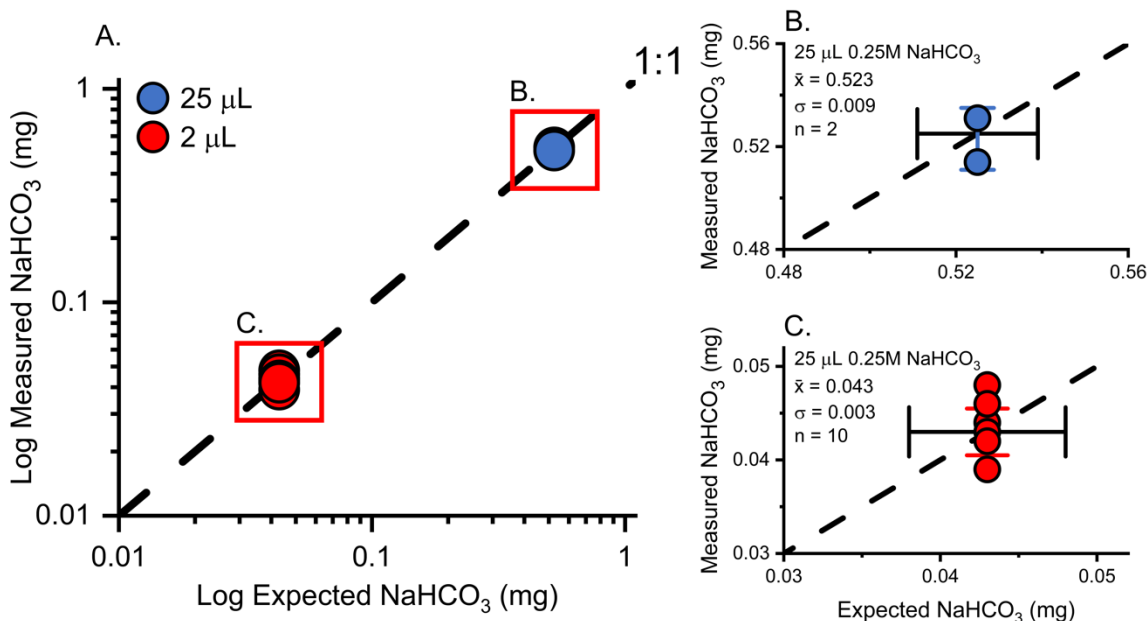


Figure 1. Experimental procedure in this study. (A) Low vacuum (10^{-3} mbar) depressurization experiment setup for the 25 and 2 μL of 0.25 M NaHCO_3 . Video for the low-vacuum depressurization experiment is linked to the “data availability” section of the online version. Note the decrepitation time is rapid (~ 5 ms). (B) Experimental pressure vessel setup for growing halite in an elevated $p\text{CO}_2$ environment. The Vessel was held at 1 atm. (C) Schematic of stock solution depressurization and lab-grown halite decrepitation experimental procedure conducted under high vacuum on the quadrupole MS inlet line. (C.1) Volatiles were quantified via a stem tip release of the stock solutions (see Pettit and Schaller, 2020). (C.2) Volatiles in the inclusions of the lab-grown halite were quantified via mechanical decrepitation, releasing the entrapped volatiles from the inclusions.



894

895 **Figure 2.** Mass of the expected residual NaHCO_3 (mg) vs mass of the measured residual
 896 NaHCO_3 (mg) from the low-vacuum depressurization experiments on the 0.25 M NaHCO_3
 897 solution at 25 μL and 2 μL volumes (A). Dotted line is the 1:1 for the expected vs measured
 898 mass of the NaHCO_3 residue. Red boxes are the expanded areas for 25 μL (B) and 2 μL (C). X-
 899 axis error bars are the syringe procedural volume error and colored y-axis error bars (blue and
 900 red) are the standard deviation of the measured samples.

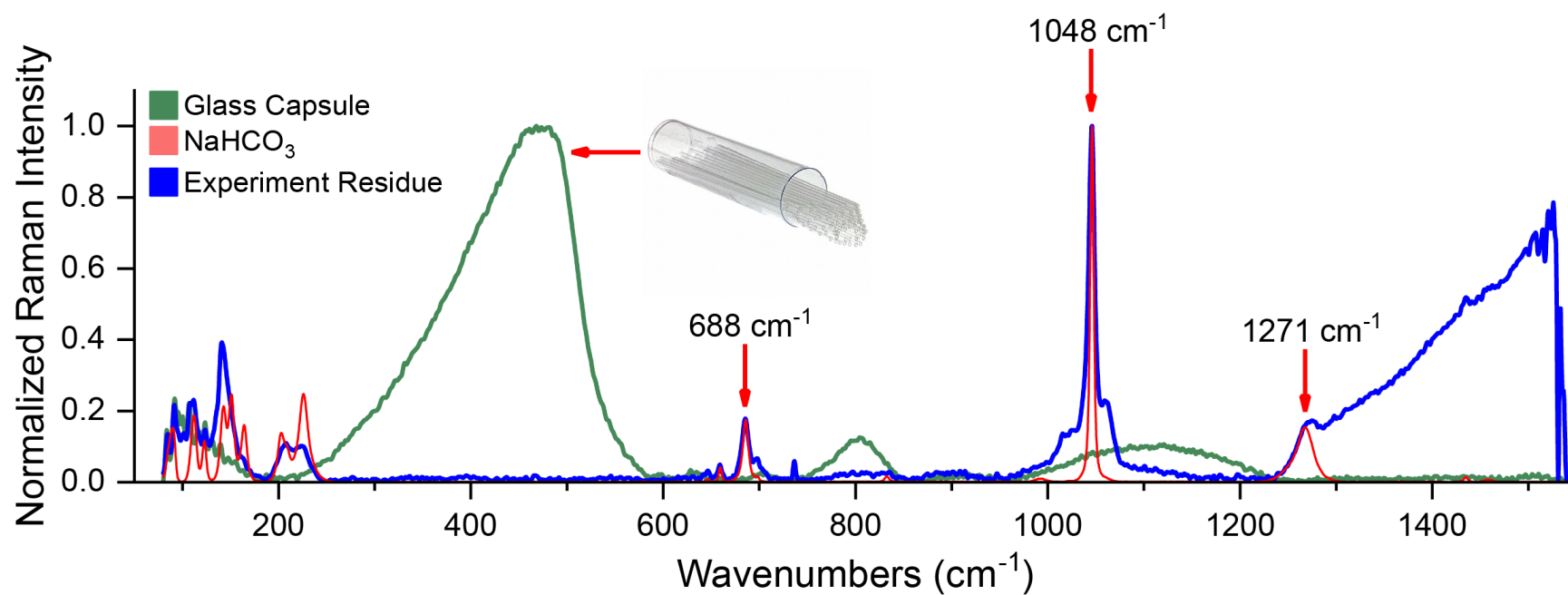


Figure 3. Raman spectra of the residue from the low-vacuum depressurization experiments. The main bands for the NaHCO₃ salt are at 688, 1048, and 1271 cm⁻¹ (pink). The spectrum of the experimental residue spectra (blue) are similar to the spectrum of the original NaHCO₃ salt, confirming the experiment residue is the original carbonate salt and is distinctly different from the spectrum of the glass microcapsule (green).

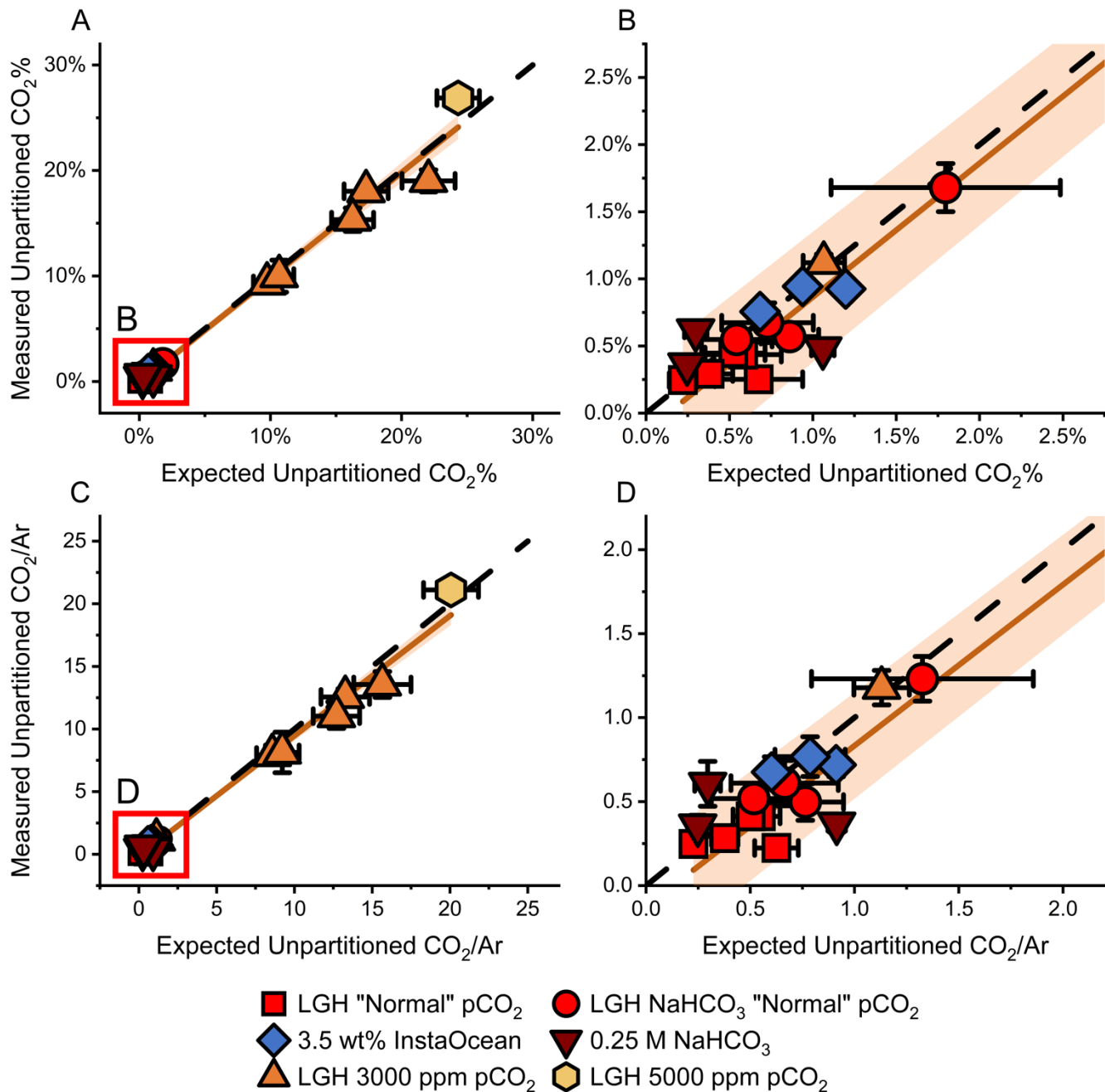


Figure 4. Results from the QMS measurements of depressurization and decrepitation experiments on the lab-grown halite (LGH) and the stock solutions. Expected vs measured CO₂ mol% (A-B) and normalized to argon (C-D) before partitioning between the aqueous and gaseous contributions. Red boxes are the expanded areas of the measured unpartitioned CO₂ mol% (B) and argon normalized CO₂ (D). Dashed line is the 1:1 of an air and air-saturated brine CO₂ mix, and the solid brown line is the linear relationship between measured and expected. Color-shaded areas are 95% confidence intervals. The error bars on the expected CO₂ were estimated based on the gas volume fraction and the range of CO₂ that the stock solutions and LGH were equilibrated under. The error bars on the measured CO₂ content are propagated uncertainties at the 95% confidence interval.

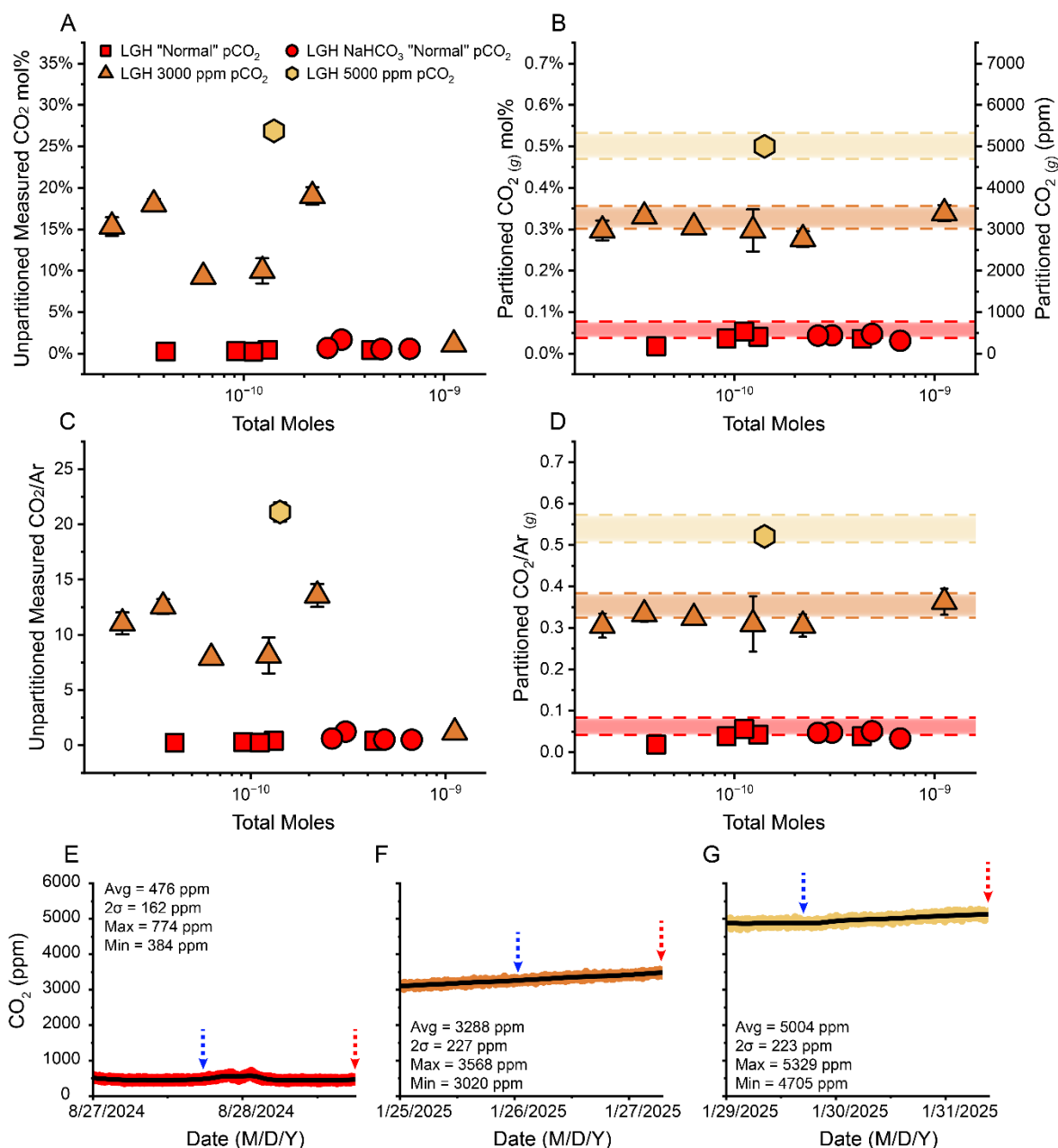


Figure 5. Total moles of measured gas (e.g., the sum of N₂, O₂, Ar, CO₂) versus the unpartitioned (A, C) and partitioned (B, D) CO₂ mol% and argon normalized CO₂ results from measurements of the lab-grown halite (LGH) decrepitation experiments. MAGPI was used to partition the raw inclusion data (Park and Schaller, 2025). Gas partitioned CO₂ measurements are compared to the monitored pCO₂ levels. LGH precipitated under “normal” (red, E) and elevated to 3000 ppm, (orange, F) and 5000 ppm (yellow, G) conditions. Blue vertical arrows represent the time points when hopper crystals were first observed during halite precipitation and red vertical arrows represent the time points when halite crystals were collected. Note that the LGH tracks the CO₂ concentration of the atmosphere with which the solutions were equilibrated and that partitioning of inclusion data is necessary for accurate interpretations. The error bars are propagated uncertainties.

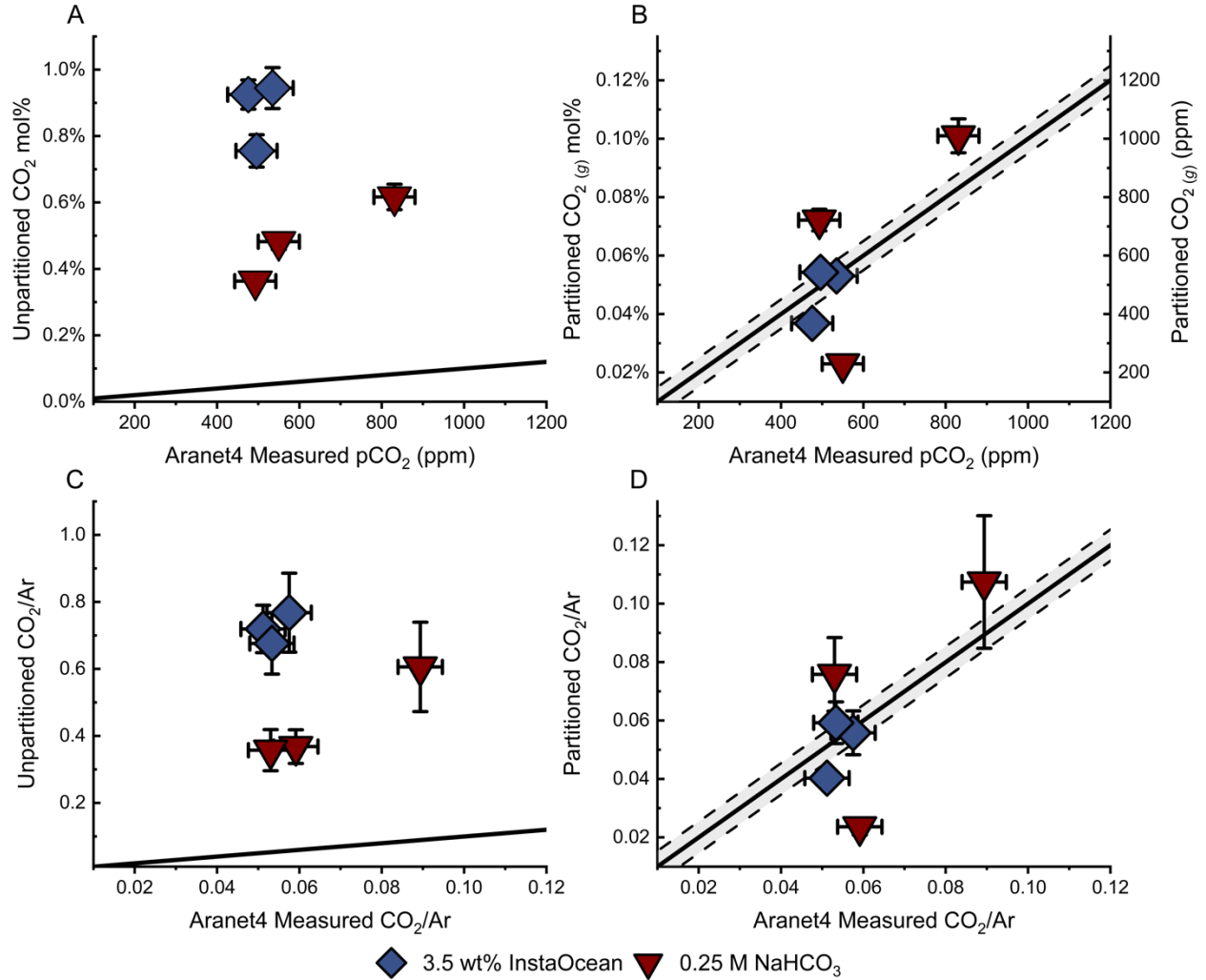


Figure 6. Measured $p\text{CO}_2$ (ppm) under which the solutions equilibrated vs. the unpartitioned (A, C) and partitioned (B, D) CO₂ mol% or CO₂/Ar from the solution depressurization experiments. The $p\text{CO}_2$ was measured by the Aranet4 CO₂ meter before the setup of each stock solution depressurization experiment. The argon to which the CO₂ was normalized was assumed to be at 0.93% in the laboratory. The solid black line is the 1:1 between the Aranet4 measured CO₂ and the QMS measured CO₂ mol% and CO₂/Ar. Dashed lines and grey shaded area are the error associated with the uncertainty in the Aranet4 CO₂ measurements at this range ($\pm 3\%$). The unpartitioned CO₂ noticeably diverges from the 1:1 line. However, the data partitioned using MAGPI (Park and Schaller, 2025) closely aligns with the 1:1 line. X-axis error is the CO₂ error of the Aranet4 and the y-axis error are propagated uncertainties.

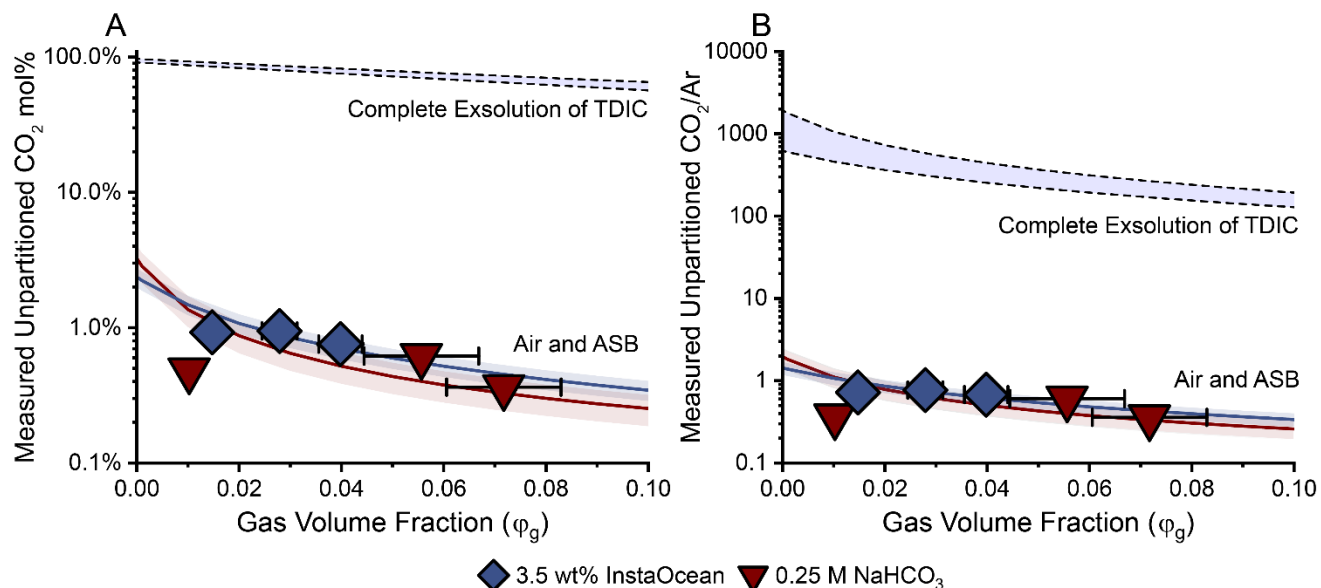


Figure 7. Results from the depressurization experiments. Measured gas volume fraction vs unpartitioned CO_2 mol% (log scale) (A) and argon normalized (B) on the 3.5 wt% InstaOcean (diamonds) and 0.25 M NaHCO_3 (inverted triangles) solutions. Solid blue and burgundy lines are the modeled expected values if the measured CO_2 represents a mix between air and air-saturated brine (ASB) for a NaCl and NaHCO_3 dominated solutions, respectively. Shaded blue and burgundy areas are the associated error for each air and ASB model. The upper and lower dotted black lines are the model values where the measured CO_2 represents the complete exsolution of total dissolved inorganic carbon (TDIC) for a NaCl and NaHCO_3 dominated solution, respectively. The measured CO_2 content aligns with the expected for an air-ASB mixture. Note the prominent difference between the modeled complete exsolution of TDIC and the actual measured CO_2 . X- and Y-axis error bars are the propagated uncertainty for the gas volume fraction and the measured CO_2 , respectively.

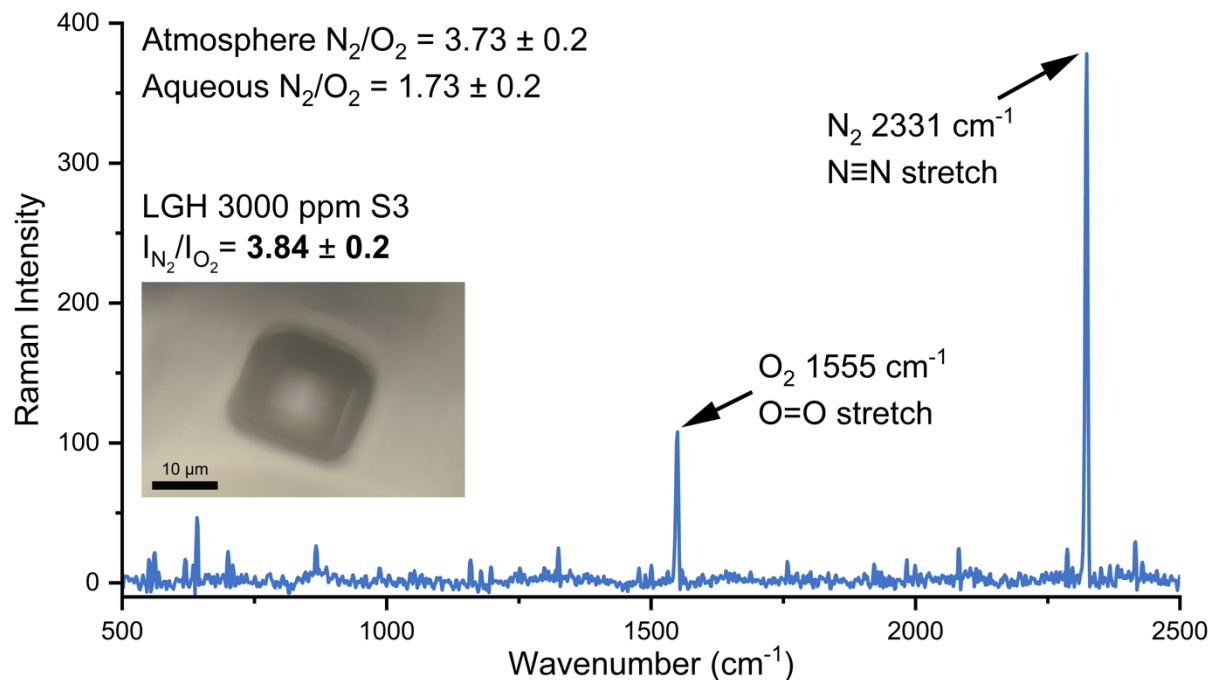


Figure 8. Raman spectrum of a fluid inclusion gas bubble in the lab-grown halite (LHG) that precipitated in ‘zero air’ (nominal atmospheric ratio of N_2 , O_2 and Ar) with a maximum pCO_2 level of 3568 ± 107 and minimum pCO_2 of 3020 ± 91 ppm. The main N_2 and O_2 peaks are present at 2331 and 1555 cm^{-1} , respectively. The ratio between the intensities of the N_2 and O_2 peaks (3.84 ± 0.24) closely matches the gaseous N_2/O_2 endmember (3.73 ± 0.2) under which the LGH precipitated and does not overlap with the aqueous N_2/O_2 endmember (1.73 ± 0.2).

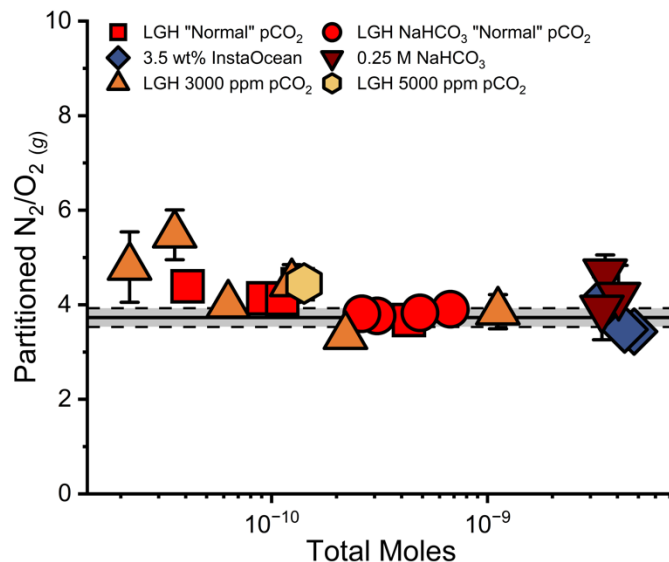


Figure 9. Partitioned $N_2(g)$ normalized to $O_2(g)$ results from the stock solution depressurization and the lab-grown halite (LGH) decrepitation experiments vs. total moles (sum of the measured N_2 , O_2 , Ar, and CO_2). Partitioned N_2/O_2 ratio of measurements is compared to the expected N_2/O_2 of the atmosphere under which the stock solutions and LGH equilibrated (solid black line). Dashed black lines and grey shaded area are the error range of N_2/O_2 for LGH precipitation. Stock solutions were equilibrated in open laboratory air and assumed N_2 was 78.08% and O_2 was 20.95%. Note that data converges to the atmospheric N_2/O_2 value (3.73). Error bars are the propagated uncertainties.

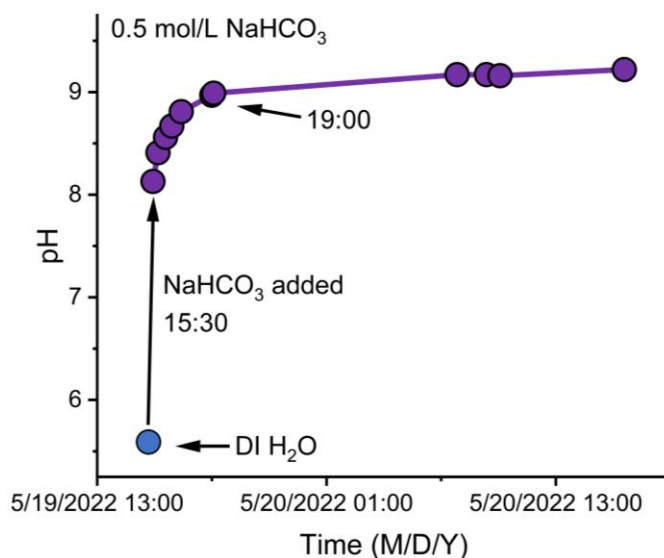


Figure 10. A 0.5 M $NaHCO_3$ solution was prepared to determine the time for atmospheric equilibration based on pH measurements. Prior to the addition of $NaHCO_3$ (blue), the pH of DI H_2O was ~ 5.5 . When $NaHCO_3$ was added (purple), the solution reached pH equilibrium with the atmosphere after ~ 3.5 hours. Time is recorded in the 24-hour format with the time in month/days/years.

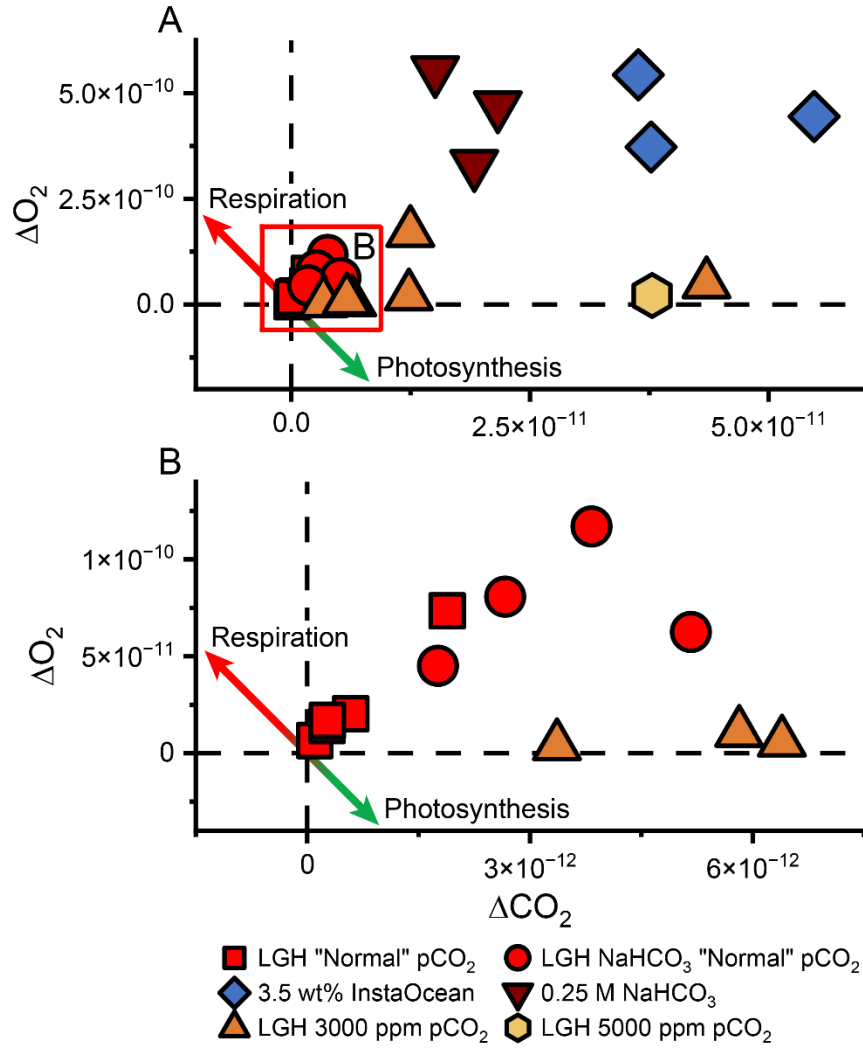


Figure 11. (A) Difference between measured and expected moles of CO_2 and O_2 in the stock solutions and lab-grown halite (LGH). Delta values are calculated relative to the modern atmospheric ratio using equation (6). (B) The expanded area of the red box in A. Green and red lines are the 1:1 expectation for stoichiometric exchange by photosynthesis and respiration, respectively. Black dashed lines represent the origin. Note that the positive relationship between pCO_2 and pO_2 is expected for solutions with different amounts of total gas.

Table 1. Forward and reverse kinetic reaction rate constants for Eq. 1a-f

Reaction	Reaction direction	magnitude	Reference
Eq. 1a	k_{+1}	$1.6 \cdot 10^{-5} \text{ s}^{-1}$	calculated
	k_{-1}	$4.1 \cdot 10^{-4} \text{ s}^{-1}$	Choi et al. (1998)
Eq. 1b	k_{+2}	$1 \cdot 10^4 \text{ M}^{-1} \cdot \text{s}^{-1}$	Eigen et al. (1961)
	k_{-2}	18.3 s^{-1}	Eldik and Palmer (1982)
Eq. 1c	k_{+3}	Instantaneously	Kern (1960)
	k_{-3}	Instantaneously	Kern (1960)
Eq. 1d	k_{+4}	59.4 s^{-1}	Zeebe and Wolf-Gladrow (2001)
	k_{-4}	$5 \cdot 10^{10} \text{ M}^{-1} \cdot \text{s}^{-1}$	Eigen et al. (1961)
Eq. 1e	k_{+5}	0.037 s^{-1}	Johnson (1982)
	k_{-5}	$2.66 \cdot 10^4 \text{ M}^{-1} \cdot \text{s}^{-1}$	Zeebe and Wolf-Gladrow (2001)
Eq. 1f	k_{+6}	$4.05 \cdot 10^3 \text{ M}^{-1} \cdot \text{s}^{-1}$	Johnson (1982)
	k_{-6}	$1.76 \cdot 10^{-4} \text{ s}^{-1}$	Zeebe and Wolf-Gladrow (2001)

Table 2. Measured mass of the residue from the low-vacuum depressurization experiments compared to the residue mass expected from the syringe on the 0.25 M NaHCO_3 solutions at 2 and 25 μL .

0.25M NaHCO_3	Measured Residue (mg)	Syringe Procedural Range (mg)
2 μL (n=10)	0.043 ± 0.003	0.043 ± 0.003
25 μL (n=2)	0.523 ± 0.009	0.525 ± 0.014

Table 3. Correlations between the measured vs. expected unpartitioned CO_2 mol% and CO_2/Ar , and ANOVA and ANCOVA results with F-test and associated p-value of the measured unpartitioned CO_2 mol% and CO_2/Ar compared to the 1:1. Bolded values are significant.

	Equation	R^2	ANOVA		ANCOVA	
			F	p(α)	F	p(α)
Unpartitioned CO_2 mol%	$y=0.99x-0.001$	0.99	0.004	0.95	0.57	0.45
Unpartitioned CO_2/Ar	$y=0.96x-0.13$	0.99	0.027	0.87	4.72	0.04

Table 4. Comparisons between the average and standard deviation of the CO₂ content before and after applying the gas-aqueous partition to lab-grown halite (LGH). Partitioned compositions closely match the compositions under which the LGH equilibrated.

Samples	CO ₂ mol%	CO ₂ /Ar
LGH “Normal” pCO₂ (n=5)		
Unpartitioned	0.3346 ± 0.0993	0.3156 ± 0.0906
Partitioned	0.0367 ± 0.0127	0.0387 ± 0.0134
LGH NaHCO₃ “Normal” pCO₂ (n=4)		
Unpartitioned	0.8680 ± 0.5440	0.7143 ± 0.3481
Partitioned	0.0414 ± 0.0072	0.0443 ± 0.0078
LGH ~3000 ppm pCO₂ (n=6)		
Unpartitioned	12.1307 ± 6.7298	9.0663 ± 4.4880
Partitioned	0.3077 ± 0.0232	0.3235 ± 0.0224
LGH ~5000 ppm pCO₂ (n=1)		
Unpartitioned	26.879	21.1087
Partitioned	0.5001	0.5208
Aranet4 CO₂	Minimum	Maximum
LGH “Normal” pCO₂	0.0384 ± 0.0012	0.0774 ± 0.0023
LGH ~3000 ppm pCO₂	0.3020 ± 0.0091	0.3568 ± 0.0107
LGH ~5000 ppm pCO₂	0.4705 ± 0.0141	0.5329 ± 0.0160

Table 5. Comparisons between the average and standard deviation of the CO₂ content of stock solutions both before and after applying the gas-aqueous partition. Partitioned compositions closely match the compositions in which the stock solutions equilibrated under.

Samples	CO ₂ mol%	CO ₂ /Ar
3.5 wt% InstaOcean (n=3)		
Unpartitioned	0.8750 ± 0.1044	0.7211 ± 0.0460
Partitioned	0.0480 ± 0.0097	0.0518 ± 0.0101
0.25 M NaHCO₃ (n=3)		
Unpartitioned	0.4873 ± 0.1271	0.4439 ± 0.1405
Partitioned	0.0654 ± 0.0395	0.0689 ± 0.0423